Atmospheric
Chemistry
and Physics
Discussions

1 **Black carbon-induced snow albedo reduction over the Tibetan Plateau: Uncertainties from**

2 **snow grain shape and aerosol-snow mixing state based on an updated SNICAR model**

3

4 Cenlin He[1,2], Mark G. Flanner[3], Fei Chen[2,4], Michael Barlage[2], Kuo-Nan Liou[5], Shichang Kang[6,7],

5 Jing Ming[8], and Yun Qian[9]

6

7 [1]Advanced Study Program, National Center for Atmospheric Research, Boulder, CO, USA

8 [2]Research Applications Laboratory, National Center for Atmospheric Research, Boulder, CO, USA

9 [3]Department of Climate and Space Sciences and Engineering, University of Michigan, Ann Arbor, MI,

10 USA

11 [4]State Key Laboratory of Severe Weather, Chinese Academy of Meteorological Sciences, Beijing, China

12 [5]Department of Atmospheric and Oceanic Sciences, University of California, Los Angeles, CA, USA

13 [6]State key laboratory of Cryospheric Science, Northwest Institute of Eco-Environment and Resources,

14 Chinese Academy of Sciences, Lanzhou, China

15 [7]CAS Center for Excellence in Tibetan Plateau Earth Sciences, Beijing, China

16 [8]Multiphase Chemistry Department, Max Planck Institute for Chemistry, Mainz, Germany

17 [9]Atmospheric Sciences and Global Change Division, Pacific Northwest National Laboratory, Richland,

18 WA, USA

19

20 *The National Center for Atmospheric Research is sponsored by the National Science Foundation.

21

22

23

24 *Correspondence to*: Cenlin He (cenlinhe@ucar.edu)

25

26

27

28

29

30

31

32

Atmospheric
Chemistry
and Physics
Discussions

Abstract

We implement a set of new parameterizations into the widely used SNow, ICe, and Aerosol Radiative (SNICAR) model to account for effects of snow grain shape (spherical versus nonspherical) and black carbon (BC)-snow mixing state (external versus internal). We find that nonspherical snow grains lead to higher pure albedo but weaker BC-induced albedo reductions relative to spherical snow grains, while BC-snow internal mixing significantly enhances albedo reductions relative to external mixing. The combination of snow nonsphericity and internal mixing suggests an important interactive effect on BC-induced albedo reduction. Comparisons with observations of clean and BC-contaminated snow albedo show that model simulations accounting for both snow nonsphericity and BC-snow internal mixing perform better than those using the common assumption of spherical snow grains and external mixing. We further apply the updated SNICAR model with comprehensive *in-situ* measurements of BC concentrations in the Tibetan Plateau snowpack to quantify the present-day (2000–2015) BC-induced snow albedo effects from a regional and seasonal perspective. The BC concentrations show distinct and substantial sub-regional and seasonal variations, with higher values in the non-monsoon season and low altitudes. As a result, the BC-induced regional mean snow albedo reductions and surface radiative effects vary by up to an order of magnitude across different sub-regions and seasons, with values of 0.7–30.7 (1.4–58.4) W m^{-2} for BC externally mixed with fresh (aged) snow spheres. The BC radiative effects are further complicated by uncertainty in snow grain shape and BC-snow mixing state. BC-snow internal mixing enhances the mean albedo effects over the plateau by 30–60% relative to external mixing, while nonspherical snow grains decrease the mean albedo effects by up to 31% relative to spherical grains. Based on this study, extensive measurements and improved model characterization of snow grain shape and aerosol-snow mixing state are urgently needed in order to precisely evaluate BC-snow albedo effects.

Atmospheric
Chemistry
and Physics
Discussions

1. Introduction

Snow albedo, a critical element in the Earth and climate system, can be significantly affected by light-absorbing impurities in snow (Warren and Wiscombe, 1980; Hansen and Nazarenko, 2004; Jacobson, 2004; Flanner et al., 2009; Liou et al., 2014), which further influences surface energy flux and regional hydrological cycles (Menon et al., 2010; Qian et al., 2011, 2015) through a positive snow albedo feedback (Qu and Hall, 2006). With the strongest light-absorbing ability, black carbon (BC) has been identified as one of the most important contributors to snow albedo reduction and snow melting after its deposition onto global snowpack (Ramanathan and Carmichael, 2008; Bond et al., 2013), including over the Arctic (McConnell et al., 2007; Meinander et al., 2013), North American mountains (Qian et al., 2009; Sterle et al., 2013; Skiles and Painter, 2016; Wu et al., 2018), European glaciers (Painter et al., 2013; Di Mauro et al., 2017), Asian seasonal snowpack (Wang et al., 2013, 2017; Zhao et al., 2014), and the Tibetan Plateau (Xu et al., 2009; Qian et al., 2011; Wang et al., 2015; Lee et al., 2017; Li et al., 2017, 2018; Zhang et al., 2017a, b, 2018). In addition, snow albedo can be affected by snow grain size, grain shape, and snowpack structures (Wiscombe and Warren, 1980; Flanner et al. 2007; Kokhanovsky, 2013; Liou et al., 2014; Qian et al., 2014; He et al., 2017a; Räisänen et al., 2017), which complicates the BC-snow-radiation interactions. Thus, it is critically important to account for the effects of snow grain properties and BC particles in order to accurately estimate snow albedo and subsequent hydro-climatic impacts.

The Tibetan Plateau (TP), also known as the Third Pole, is covered by the largest mass of snow and ice outside the Arctic and Antarctic (Kang et al., 2010; Yao et al., 2012). It is the source region of major Asian rivers, providing fresh water for billions of people (Qin et al., 2006; Immerzeel et al., 2010). Meanwhile, because of its thermal heating, the TP has profound dynamical influences on the atmospheric circulation in the Northern Hemisphere and long been identified to be critical in regulating the Indian and East Asian monsoons (Manabe and Terpstra, 1974; Yeh et al., 1979; Yao et al., 2012). The TP is very sensitive to the change in snow albedo and cover, which alter surface heat and water balances and further disturb the Asian hydrological cycle and monsoon climate (Kang et al., 2010). Observations have shown substantial BC concentrations in snow over the TP and suggested that BC deposition is an important driver of strong albedo reductions and accelerated glacier retreat in the region (Ming et al., 2008, 2013; Xu et al., 2009; Qu et al., 2014; Ji et al., 2015; Niu et al., 2017; Li et al., 2017b; Zhang et al., 2018). Recent studies found that BC

Atmospheric
Chemistry
and Physics
Discussions

95   particles over the TP are primarily from South and East Asia, while long-range transport from

96   northern mid-latitudinal source regions outside Asia also has nontrivial contributions (Kopacz et

97   al. 2011; Lu et al., 2012; He et al., 2014a, b; Zhang et al., 2015; Li et al., 2016; Yang et al., 2018).

98   To estimate BC-induced snow albedo effects over the TP, previous studies often used

99   observed BC concentrations in snow/ice as inputs to snow albedo models by assuming spherical

100   snow grains and BC-snow external mixing (e.g., Ming et al., 2013; Jacobi et al., 2015; Schmale et

101   al., 2017; Zhang et al., 2018). This simplified treatment of BC-snow interactions has been widely

102   used in snow albedo modeling over various snow-covered regions (e.g., Warren and Wiscombe,

103   1980; Flanner et al., 2007; Aoki et al., 2011). However, snow grains are usually nonspherical

104   (Dominé et al., 2003) and internally mixed with BC particles (Flanner et al., 2012) in real

105   snowpack, which could significantly affect BC-snow albedo effects. For example, Kokhanovsky

106   and Zege (2004) pointed out that substantial errors could occur if assuming spherical snow grains

107   in albedo modeling. Dang et al. (2016) found that, compared with spherical snow grains, the

108   nonspherical counterparts lead to higher pure snow albedo but smaller BC-induced albedo

109   reduction for BC-snow external mixing. In addition, Flanner et al. (2012) showed that there could

110   be up to 73% of BC in global snowpack internally mixed with snow grains, which increases BC-

111   induced albedo effects by up to 86% relative to purely external mixing for spherical snow grains.

112   Moreover, recent studies (He et al., 2014b, 2018a; Liou et al., 2014), combining both effects of

113   snow nonsphericity and BC-snow internal mixing, revealed that the enhancement in snow albedo

114   reduction caused by internal mixing can be weakened by snow nonsphericity effect. Therefore,

115   ignoring these two critical factors in previous studies could lead to biased estimates of BC-induced

116   snow albedo effects over the TP and elsewhere, which highlights the necessity of accounting for

117   the two features together in snow albedo modeling and assessing the associated uncertainty.

118   In this study, we implement a set of new BC-snow parameterizations (He et al., 2017b)

119   into the widely used SNow, ICe, and Aerosol Radiative (SNICAR) model (Flanner et al., 2007) to

120   consider the effects of snow nonsphericity and BC-snow internal mixing. We further apply the

121   updated SNICAR model with a comprehensive set of *in-situ* measurements of BC concentrations

122   in the TP snowpack to estimate the present-day (2000-2015) BC-induced snow albedo effects and

123   associated uncertainties from snow grain shape (spherical versus nonspherical) and BC-snow

124   mixing state (external versus internal) from a regional and seasonal perspective. To the best of our

125   knowledge, this is the first attempt to quantify BC-snow albedo effects over the TP by taking into

126   account the aforementioned two factors concurrently with observational constraints. We describe

127   BC observations in the TP snowpack in Section 2. We implement the BC-snow parameterizations

128   and evaluate model results in Section 3. We further quantify and discuss the BC-snow albedo

129   effects and associated uncertainties in Section 4. Finally, we present conclusions, implications,

130   and future work in Section 5.

131

132   **2. BC observations in the Tibetan snowpack**

133   We collect available *in-situ* observations of BC concentrations in snow/ice over the TP and

134   surrounding areas during 2000–2015 from historical measurements (see Table S1 for summary).

135   Although the features of BC concentrations at each site have been described in detail by previous

136   observational studies, the present analysis seeks to summarize all these measurements in order to

137   understand the regional and seasonal characteristics of BC pollution in the TP snowpack and more

138   importantly to estimate the corresponding BC-snow albedo effects and associated uncertainties

139   due to snow grain shape and BC-snow mixing state using an updated snow model (see Section 3).

140   For detailed analyses, we divide the entire TP and surrounding areas into six sub-regions

141   (Fig. 1), including northwestern TP (NWTP; 34–40°N, 70–78°E), north of TP (NOTP; 40–45°N,

142   70–95°E), northeastern TP (NETP; 34–40°N, 95–105°E), southeastern TP (SETP; 27–34°N, 95–

143   105°E), central TP (CTP; 30–36°N, 78–95°E), and the Himalayas (HIMA). We note that NOTP

144   represents the Tianshan region. Due to its proximity to the TP, we analyze it together with the TP

145   snowpack in this study. Moreover, BC concentrations in the TP snowpack show distinct altitudinal

146   and seasonal variations within each sub-region (Figs. 1a–1f), with much larger values at relatively

147   lower altitudes (<5200 m a.s.l.) and in the non-monsoon season (October–May; Xu et al., 2009),

148   compared with higher altitudes (>5200 m a.s.l.) and the monsoon season (June–September; Xu et

149   al., 2009), respectively. Thus, we conduct analyses according to different altitudes (above or below

150   5200 m a.s.l.) and seasons (monsoon or non-monsoon). In addition, for any observational site with

151   multiple measurements during the same season, we average the measurements to represent the

152   mean BC pollution condition for this site during the season. Since a rather limited number of sites

153   provide vertically resolved BC measurements throughout snowpack, we average BC

154   concentrations throughout snow layers at these sites, which may introduce some uncertainties.

155   Figures 1a–1f show that BC concentrations in snow are generally much higher during the

156   non-monsoon period than during the monsoon period by up to one order of magnitude, except for

157   NWTP and NOTP. This is because the four sub-regions (NETP, SETP, CTP, and HIMA) are

158   dominated by the strong BC emissions in the non-monsoon season (particularly winter and spring)

159   over South and East Asia (Lu et al., 2012; Zhang et al., 2015; Yang et al., 2018) and the efficient

160   wet removal of BC in Asia in the monsoon season (Xu et al., 2009; He et al., 2014a). In contrast,

161   the high concentrations during the monsoon period over NWTP and NOTP are primarily caused

162   by the enrichment of BC via sublimation and/or melting of snow (Ming et al., 2009; Yang et al.,

163   2015) and emissions from Central Asia and Middle East (Kopacz et al., 2011; Schmale et al.,

164   2017).

165   Furthermore, BC concentrations are consistently larger at low altitudes (<5200 m) than at

166   high altitudes (>5200 m) by a factor of 2–10 in each sub-region (Figs. 1a–1f), which is consistent

167   with previous studies (Ming et al., 2009, 2013) which suggested that BC concentrations decrease

168   with increasing elevations. Such altitudinal contrast in BC concentrations are maximal (with

169   differences larger than one order of magnitude) over HIMA and SETP. This elevational

170   dependence can be attributed to the stronger local emissions at lower elevations, the reduced

171   efficiency of BC transport to higher elevations, and the higher temperature at lower elevations

172   leading to stronger snow melting and hence BC enrichment in snow (e.g., Ming et al., 2013; Niu

173   et al., 2017; Zhang et al., 2018).

174   Among the six sub-regions, the high-altitude areas in HIMA and SETP show the lowest

175   BC concentrations (5–30 ppb) throughout the year (Figs. 1d–1f), while NETP (with only low-

176   altitude sites) during the non-monsoon season is most severely polluted by BC (~4300 ppb). The

177   results further indicate that BC concentrations in low-altitude areas across different sub-regions

178   are comparable (190–450 ppb) during the monsoon season but are much more variable during the

179   non-monsoon season (Figs. 1d–1f). The variation of BC concentrations across the sub-regions is a

180   result of combined effects of the aforementioned factors (e.g., regionally and seasonally dependent

181   impacts from BC source, transport, removal, and snow aging). We note that the current

182   observations over the TP are still rather limited spatially and temporally, leading to questions of

183   representativeness and introducing uncertainty in the analysis. Thus, the large sub-regional,

184   altitudinal, and seasonal heterogeneity of BC concentrations in the TP snowpack highlights an

185   urgent need for extensive measurements.

186

187   **3. Model description, implementation, and evaluation**

3.1 SNICAR model

188

189   Flanner et al. (2007) developed a multi-layer SNow, ICe, and Aerosol Radiative (SNICAR)

190 model, which has been widely used for snowpack simulations globally. It is also coupled to global

191 climate models (e.g., Community Earth System Model, CESM) to investigate effects of impurity

192 contamination, snow grain properties, and snow aging on snowpack albedo. A detailed model

193 description has been presented by Flanner et al. (2007) and implementation in CESM is described

194 by Oleson et al. (2013). Here we briefly summarize the key model elements related to the present

195 study. SNICAR simulates snowpack radiative transfer based on the theory from Wiscombe and

196 Warren (1980) and the multi-layer two-stream radiative transfer solution from Toon et al. (1989).

197 It resolves vertical distributions of snow properties, impurity distributions, and heating throughout

198 the snowpack column, as well as impact of underlying ground surfaces. The number of snow layers

199 can be specified by users according to research objectives. The default SNICAR model assumes

200 spherical snow grains and external mixing between impurities and snow grains. As inputs to

201 radiative transfer calculations, the optical properties (extinction cross section (Q_{ext}), single-

202 scattering albedo (ω), and asymmetry factor (g)) of snow grains and impurities, archived as lookup

203 tables, are offline computed by the Mie theory based on particle size distributions and refractive

204 indices. SNICAR utilizes clear- and cloudy-sky surface incident solar flux typical of mid-latitude

205 winter. The input parameters for SNICAR include incident radiation type (direct/diffuse), solar

206 zenith angle, number of snow layers with thickness, density, and grain effective radius in each

207 layer, underlying ground albedo, and aerosol concentrations in snow. In this study, we use the

208 stand-alone version of SNICAR (available at http://snow.engin.umich.edu/snicarcode/) and

209 implement new parameterizations of snow nonsphericity and BC-snow internal mixing into it (see

210 Sections   3.2   and   3.3).   The   updated   SNICAR   model   is   available   at

211 https://github.com/EarthSciCode/SNICARv2.

212

3.2 Implementation of nonspherical snow grains

213

214   Previous studies commonly used an effective spherical snow grain with an equal volume-

215 to-area ratio (i.e., equal surface area-weighted mean radius; hereinafter effective radius, R_e) to

216 represent its nonspherical counterpart (e.g., Fu et al., 1999; Grenfell et al., 2005). The equal-

217 effective-radius representation works well in computing extinction efficiency and single-scattering

218 albedo but is inaccurate for asymmetry factor (Dang et al., 2016). To explicitly resolve snow grain

219   shapes, Liou et al. (2014) have developed a stochastic snow albedo model based on a geometric-

220   optics surface-wave (GOS) approach (Liou et al., 2011; He et al., 2015, 2016; Liou and Yang,

221   2016). Further, He et al. (2017b) developed a parameterization to account for snow nonsphericity

222   effects on asymmetry factors for three typical grain shapes, including spheroid, hexagonal plate,

223   and Koch snowflake (see Fig. 1 of He et al. 2017b). They parameterized the asymmetry factor (g_{ns})

224   of nonspherical snow grains as follows:

$$g_{ns} = g_{hex} \times C_{g} \tag{1}$$

$$C_{g} = a_0 \left(\frac{f_{s,x}}{f_{s,hex}} \right)^{a_1} (2R_s)^{a_2} \tag{2}$$

227   where a_i ($i = 0$–2) is the wavelength-dependent coefficient available in He et al. (2017b). R_s (unit:

228   μm) is equal to the snow effective radius (R_e) for spheroid or hexagonal plate, and $R_e/0.544$ for

229   Koch snowflake due to its complex concave shape. $f_{s,x}$ and $f_{s,hex}$ are the shape factors (i.e., ratio

230   of R_s of a nonspherical grain to that of an equal-volume sphere) of a nonspherical grain (x:

231   spheroid, hexagonal plate, or Koch snowflake) and hexagonal plate, respectively. C_g is the

232   correction factor, and g_{hex} is the asymmetry factor for hexagonal shapes computed as follows (Fu,

233   2007):

$$g_{hex} = \frac{1-g'}{2\omega} + g' \tag{3}$$

$$g' = b_0 + b_1 \times AR + b_2 \times AR^2, \quad \text{for } 0.1 \leq AR \leq 1.0 \tag{4a}$$

$$g' = c_0 + c_1 \times \ln(AR) + c_2 \times \ln^2(AR), \quad \text{for } 1.0 < AR \leq 20 \tag{4b}$$

237   where ω is the snow single-scattering albedo, and g' is the asymmetry factor related to geometric

238   reflection and refraction. b_i and c_i ($i = 0$–2) are the wavelength-dependent coefficients available in

239   Fu (2007). AR is the snow aspect ratio (i.e., ratio of grain width to length).

240   Here we implement the He et al. (2017b) parameterization (Equations 1–4) for snow

241   asymmetry factor into SNICAR to account for nonspherical shapes. Due to the coarse spectral

242   resolution (6 bands) of the parameterization, we further use a piece-wise shape-preserved

243   polynomial interpolation method (Fritsch and Carlson, 1980) to interpolate the parameterized

244   results into 470 bands (0.3–5 μm with a 10-nm resolution) used in SNICAR. The same

245   interpolation method is also applied to implementing the single-scattering co-albedo

246   parameterization for BC-contaminated snow (see Section 3.3). We use the extinction efficiency

247   and single-scattering albedo of equal-effective-radii spheres for those of the nonspherical grains.

Atmospheric
Chemistry
and Physics
Discussions

248   Figures 2a–2c show the spectral snow asymmetry factors for different grain shapes based

249   on the updated SNICAR model. Compared with spherical snow grains, nonspherical grains

250   (particularly Koch snowflakes) result in up to ~17% smaller asymmetry factors at wavelengths <

251   ~3.0 μm, consistent with previous studies (Liou et al., 2014; Dang et al., 2016). We note that the

252   results slightly (<3%) overestimate the asymmetry factors at two spectral peaks within 1.5–2.5 μm

253   for spheroids with large sizes ($R_e \geq 500$ μm), due to parameterization uncertainties (He et al.,

254   2017b).

255   As a result of the smaller asymmetry factors, nonspherical snow grains lead to weaker

256   forward scattering and hence higher albedo relative to their spherical counterparts (Figs. 3 and S1).

257   We find up to about 2% and 27% higher albedo for Koch snowflakes in the visible (0.3–0.7 μm)

258   and near-infrared (NIR, 0.7–5 μm) bands, respectively, compared to equal-R_e spheres (Figs. 3d

259   and 3e). These results show good agreement with the conclusions from previous studies (Wang et

260   al., 2017; He et al., 2018a). The results also have important implications for snow grain size

261   retrievals via the use of albedo models to match observed spectral reflectance. For example, Dang

262   et al. (2016) and He et al. (2018a) suggested that if a nonspherical grain is simulated as a sphere,

263   its effective size has to be scaled down by a factor of 1.2–2.5 to obtain the correct snow albedo.

264

265   **3.3 Implementation of BC-snow internal mixing**

266   Flanner et al. (2012) showed that the effect of BC-snow internal mixing can be equivalent

267   to applying an enhancement ratio to BC absorption cross sections with the external mixing

268   assumption and developed a lookup table for the enhancement ratio. Recently, He et al. (2017b)

269   explicitly resolved the structures of BC-snow internal mixtures for different snow shapes and

270   found that inclusions of BC increase snow single-scattering co-albedo (1-ω) and hence absorption

271   but have negligible effects on snow asymmetry factor and extinction efficiency. They further

272   parameterized the effect of internal mixing on 1-ω as follows:

273    $$E_{1-\omega} = d_0 \times (C_{BC} + d_2)^{d_1} \qquad (5)$$

274   where $E_{1-\omega}$ is the co-albedo enhancement defined as the ratio of single-scattering co-albedo for

275   BC-contaminated snow to that for pure snow, which is a function of BC mass concentration in

276   snow (C_{BC}, unit: ppb). d_i ($i = 0$–2) is the wavelength-dependent parameterization coefficient

277   available in He et al. (2017b).

Atmospheric
Chemistry
and Physics
Discussions

278   Here we implement the He et al. (2017b) parameterization (Equation 5) for snow single-

279   scattering co-albedo to account for BC-snow internal mixing. We note that the BC mass absorption

280   cross section (MAC) at 550 nm used in He et al. (2017b) is 6.8 m^2 g^{-1} with a BC density of 1.7 g

281   cm^{-3} and an effective radius of 0.1 μm. Thus, to obtain a BC MAC of 7.5 m^2 g^{-1} at 550 nm

282   recommended by Bond and Bergstrom (2006), we adjust the BC size and density in this study. We

283   assume a lognormal BC size distribution with a geometric mean diameter of 0.06 μm following

284   Dentener et al. (2006) and Yu and Luo (2009) and a geometric standard deviation of 1.5 following

285   Flanner et al. (2007) and Aoki et al. (2011). Then, we tune the BC density to 1.49 g cm^{-3} to match

286   the MAC (7.5 m^2 g^{-1}). The resulting BC size effect on $E_{1-\omega}$ is quantified using a parameterization

287   developed by He et al. (2018b) as follows:

288    $$E_{1-\omega,R_{BC}} = k_{\lambda,R_{BC}} \times E_{1-\omega,R_{BC}=0.05}^{f_{\lambda,R_{BC}}}$$ (6a)

289    $$\text{with } d_{\lambda,R_{BC}} = (\frac{R_{BC}}{0.05})^{m_\lambda}, \quad f_{\lambda,R_{BC}} = (\frac{R_{BC}}{0.05})^{n_\lambda}$$ (6b)

290   where $E_{1-\omega,R_{BC}}$ and $E_{1-\omega,R_{BC}=0.05}$ are the $E_{1-\omega}$ for a certain BC effective radius (R_{BC}) and a R_{BC} of

291   0.05 μm (reference case), respectively. $k_{\lambda,R_{BC}}$ and $f_{\lambda,R_{BC}}$ are empirical parameters relying on

292   wavelength and BC size. m_λ and n_λ are wavelength-dependent coefficients available in He et al.

293   (2018b).

294   Figures 2d–2f show the spectral single-scattering co-albedo of snow internally mixed with

295   BC based on the updated SNICAR model. The strongest co-albedo enhancement (up to about 4

296   orders of magnitude for 1000 ppb BC) is in the visible band, with negligible effects at wavelengths

297   >1 μm. As a result of the enhanced snow absorption, snow albedo reduces about two-fold more

298   due to internal mixing than external mixing (Figs. 4 and S2–S4). In contrast, BC decreases snow

299   albedo much less for nonspherical snow grains than spherical grains (Figs. 4 and S3–S4),

300   suggesting an important interactive effects of snow grain shape and BC-snow mixing state on snow

301   albedo reductions. For example, BC-sphere external mixing leads to similar visible albedo

302   reductions with BC-hexagonal plate internal mixing. This is consistent with our previous findings

303   (He et al., 2018a). Although the internal mixing effect dominates at the NIR wavelengths (Fig. 4e),

304   the NIR albedo reduction is a factor of 3–5 lower than the visible reduction. Thus, both snow

305   nonsphericity and BC-snow internal mixing play comparably important roles in determining all-

306   wavelength albedo reductions (Fig. 4f). This highlights the significance of simultaneously

307   accounting for these two factors in accurate estimates of BC-snow albedo effects.

Atmospheric
Chemistry
and Physics
Discussions

308   Moreover, to cross-validate model results, we compare the simulated snow albedo and its

309   reduction for BC-snow internal mixing using the He et al. (2017b) parameterization with those

310   using the Flanner et al. (2012) lookup table. We find very good agreement (mean differences <

311   3%) between the two schemes for different snow sizes and shapes (Figs. 5 and S5–S6), although

312   the He et al. (2017b) parameterization leads to slightly stronger and weaker albedo reductions for

313   higher (>1000 ppb) and lower (<1000 ppb) BC concentrations, respectively. Compared with the

314   lookup table method, the newly-implemented parameterization in this study can be applied to a

315   wider range of snow grain size, shape, and BC concentration scenarios without sacrificing

316   computational efficiency.

317

318   **3.4 Comparisons with observations**

319   **3.4.1 Pure snow albedo**

320   We evaluated spectral pure snow albedo from SNICAR simulations by comparing with

321   observations (Fig. 6) from laboratory measurements (Hadley and Kirchstetter, 2012), open-field

322   experiments (Brandt et al., 2011), and field measurements in the Rocky Mountains (Painter et al.,

323   2007) and at the South Pole (Grenfell et al., 1994). To conduct reasonable comparisons, we used

324   the observed snowpack conditions in model simulations (e.g., snow density, grain size, thickness,

325   snowpack layers, direct/diffuse light, solar zenith angle, and underlying ground albedo) and made

326   reasonable assumptions for cases when measurements are absent (see Table 1 and Figure 6). We

327   further assumed four types of snow shapes (sphere, spheroid, hexagonal plate, and Koch

328   snowflake) in the simulations to investigate shape effects, due to the lack of measurements.

329   We find that model simulations generally capture the observed patterns of spectral snow

330   albedo in all cases (Fig. 6). However, assuming spherical grains tends to underestimate snow

331   albedo in the NIR band, while using nonspherical grains improves model results. For example,

332   compared with the observations (Painter et al., 2007), simulations assuming snow spheres show a

333   systematical underestimate of up to ~0.1 at wavelengths >0.7 μm, particularly at 1.0–1.2 μm (Fig.

334   6c), while simulations assuming hexagonal plates well match the observations. Similarly, in the

335   observational case of Grenfell et al. (1994), assuming hexagonal plates and Koch snowflakes

336   substantially reduces model underestimates at 1.5–2.5 μm relative to assuming spheres, though

337   leading to a slight overestimate at 0.9–1.3 μm (Fig. 6d). In contrast, in comparison with the

338   laboratory measurements from Hadley and Kirchstetter (2012), the spherical assumption works

Atmospheric
Chemistry
and Physics
Discussions

339   reasonably well, particularly for large sizes, with only slight (<0.05) underestimates. This is

340   because the snow grains created in those experiments tend to be spherical. Nevertheless, using

341   spheroids and hexagonal plates in this case still leads to slightly better model results for large (R_e

342   = 65 and 110 µm) and small (R_e = 55 µm) grain sizes, respectively (Fig. 6a). In the observational

343   case of Brandt et al. (2011), they determined snow effective sizes by matching model results with

344   the measured NIR (1.0–1.3 µm) albedo. We find that assuming different snow shapes results in

345   drastically different grain sizes retrieved by matching their measured NIR albedo (Figs. 6b and

346   7d), with effective radii of 80 and 160 µm for spheres and Koch snowflakes, respectively. This

347   implies the necessity of accounting for realistic grain shapes in snow grain size retrievals.

348

349   **3.4.2 BC-contaminated snow albedo**

350   We further compared BC-contaminated snow albedo from SNICAR simulations with

351   observations (Fig. 7) from laboratory measurements (Hadley and Kirchstetter, 2012), open-field

352   experiments (Brandt et al., 2011; Svensson et al., 2016), and field measurements in the Arctic

353   (Meinander et al., 2013; Pedersen et al., 2015). Similar to Section 3.4.1, we used the observed

354   snowpack conditions in model simulations and made proper assumptions for cases when

355   measurements are absent (see Table 1 and Figure 7) to make reasonable comparisons. Due to the

356   lack of measurements, we assumed BC internally or externally mixed with different snow shapes

357   in the simulations to quantify the combined effects of BC-snow mixing state and snow grain shape.

358   Compared with the widely-used assumption of BC externally mixed with spherical snow

359   grains, we find that accounting for both internal mixing and snow nonsphericity improves model

360   simulations (Fig. 7). For example, assuming BC-sphere external mixing leads to a systematical

361   underestimate of polluted snow albedo for <2000 ppb BC compared with the observations from

362   Svensson et al. (2016), while assuming BC-Koch snowflake internal mixing reduces the model

363   underestimate (Fig. 7b), with the normalized mean bias (NMB) and root-mean-square error

364   (RMSE) decreasing from -0.04 to 0.01 and from 0.033 to 0.019, respectively. Similarly, in the

365   observational case of Pedersen et al. (2015), simulations assuming BC-spheroid external mixing

366   perform better than those assuming BC-sphere external mixing (Fig. 7a), reducing the NMB from

367   -0.012 to -0.003 and RMSE from 0.028 to 0.025. Compared with the observations of Meinander

368   et al. (2013), model results using spherical snow grains underestimate the spectral snow albedo

369   contaminated by BC (Fig. 7c), regardless of model assumptions of BC-snow mixing state. Using

370 nonspherical grains instead increases the simulated albedo and reduces model biases in this case,

371 although it is still unable to fully capture the observed pattern (Fig. 7c). Considering that snow

372 grains tend to be spherical in the observations from Hadley and Kirchstetter (2012), we assumed

373 BC-sphere external/internal mixing in the comparisons. The model results with external mixing

374 are systematically biased high, particularly for large BC concentrations (>110 ppb), while using

375 internal mixing effectively reduces the albedo overestimates (Fig. 7e). As such, the observations

376 fall between the results of external and internal mixing, suggesting a combination of partial

377 external and internal mixing would best match the observations. Compared with the way of

378 increasing BC MAC for BC-snow external mixing to reduce model overestimates in polluted snow

379 albedo, which was used in Hadley and Kirchstetter (2012), the present study provides a physically-

380 based alternative (i.e., internal mixing) for model improvements. In fact, it is very likely that a

381 large portion of BC is internally mixed with snow grains in the experiments of Hadley and

382 Kirchstetter (2012), since they produced the BC-contaminated snow via freezing of aqueous

383 hydrophilic BC suspensions.

384

385 **4. BC-snow albedo effects and uncertainties over the Tibetan Plateau**

386 Based on the observed BC concentrations in snow (see Section 2), we applied the updated

387 SNICAR model (see Section 3) to quantify the present-day (2000–2015) BC-snow albedo

388 reduction and associated surface radiative effects over the TP. We conducted albedo simulations

389 at each observational site using the measured snowpack thickness and density (see Table S1)

390 concurrently with BC measurements. If the snow property measurements are missing at certain

391 site, the data from nearby sites are used instead. We then computed the regional mean values by

392 averaging across all sites within each sub-region and season. We used typical effective radii of 100

393 μm and 1000 μm for fresh and aged snow, respectively, to demonstrate snow aging/size effects.

394 Due to the lack of measurements for snow grain shape and BC-snow mixing state, we considered

395 eight simulation scenarios with the combination of four snow shapes (sphere, spheroid, hexagonal

396 plate, and Koch snowflake) and two mixing states (internal and external). In the simulations, the

397 underlying ground albedo over the TP is 0.1 at the visible band (0.3–0.7 μm) and 0.2 at the NIR

398 band (0.7–5 μm), following observations (Qu et al., 2014). We adopted a solar zenith cosine of

399 0.65 (i.e., an angle of 49.5°), which is equivalent to the insolation-weighted solar zenith cosine in

400 the sunlit hemisphere. The effect of solar zenith angle on snow albedo can be approximated via

401   changing snow effective size (Marshall, 1989). Previous studies (e.g., Aoki et al., 2003; Dang et

402   al., 2016) indicated that the impact of snow shape and BC contamination decreases with an

403   increasing solar zenith angle. Following Dang et al. (2017), we compute all-sky snow albedo via

404   averages of clear- and cloudy-sky albedo weighted by cloud cover fraction. The mean cloud cover

405   fraction and all-sky surface downward solar radiation in different sub-regions and seasons (see

406   Table S2) are derived from the multi-year (2000–2015) monthly mean Modern-Era Retrospective

407   analysis for Research and Applications version 2 (MERRA-2) reanalysis meteorological fields

408   (https://gmao.gsfc.nasa.gov/reanalysis/MERRA-2/) with a spatial resolution of 0.5°×0.625°.

409   Figures 8a–8c show the regional mean BC-induced snow albedo reductions in different

410   sub-regions and seasons. The spatiotemporal distribution of albedo reductions generally follows

411   that of BC concentrations in snow (Figs. 1d–1f), with stronger albedo reductions in low-altitude

412   areas and the non-monsoon period. We find that snow albedo decreases by a factor of 2–3 more

413   for aged snow (Table S3) than for fresh snow (Table 2), due to larger grain sizes for aged snow.

414   This aging/size effect dominates the albedo reductions in most of TP sub-regions, particularly

415   during the monsoon season (Figs. 8a–8c). However, in severely polluted sub-regions including the

416   low-altitude areas of NETP, SETP, CTP, and HIMA during the non-monsoon season, the effects

417   of snow grain shape and BC-snow mixing state are comparable to those of snow size/aging (Tables

418   2 and S3). For example, BC-sphere internal mixing leads to an albedo reduction of 0.114 for fresh

419   snow in low-altitude CTP during the non-monsoon season, while BC-Koch snowflake external

420   mixing leads to a reduction of 0.119 for aged snow.

421   Moreover, BC-snow internal mixing enhances the mean albedo reductions by 30–60%

422   (relative difference) across all the sub-regions and seasons, with similar enhancements for different

423   snow shapes and sizes (Tables 2 and S3). For example, assuming BC-sphere external mixing leads

424   to an annual albedo reduction of 0.066 (0.164) for fresh (aged) snow in NETP, while the internal

425   mixing counterpart results in a reduction of 0.095 (0.225). Our results are partially different from

426   those in He et al. (2018a) which showed a stronger enhancement (relative difference) in albedo

427   reduction caused by internal mixing for nonspherical grains than spherical grains, due to different

428   environmental conditions and snow albedo models used in the two studies. We further find that

429   nonspherical snow grains weaken the mean albedo reductions by up to 31% relative to spherical

430   grains in different sub-regions and seasons, with the strongest weakening for Koch snowflakes

431 (Figs. 8a–8c). The nonsphericity effect is smaller for aged snow compared with fresh snow (Tables

432 2 and S3), consistent with our previous findings (He et al., 2018a).

433 Although the BC concentrations in the TP snowpack tend to dominate the regional and

434 seasonal pattern of snow albedo reductions for fresh/aged snow (Figs. 1d–1f and 8a–8c), the

435 combined effects of snow grain shape and BC-snow mixing state can complicate the picture. For

436 example, with the widely used assumption of BC externally mixed with snow spheres, the non-

437 monsoon albedo reductions are 0.034 and 0.067 for high-altitude CTP and low-altitude SETP with

438 BC concentrations of 332 and 1111 ppb in fresh snow, respectively. However, if BC particles were

439 internally mixed with snow spheres in CTP and externally mixed with Koch snowflakes in SETP,

440 the albedo reductions in the two areas would become the same (0.047), regardless of the

441 substantially different BC concentrations. This points toward an imperative need for both extensive

442 measurements and improved model characterization of snow grain shape and aerosol-snow mixing

443 state for accurate quantification of BC-induced snow albedo reductions over the TP and elsewhere

444 with strong heterogeneity of snowpack properties and contamination.

445 Figures 8d–8f show the regional mean surface radiative effects caused by BC-induced

446 snow albedo reductions, which vary from 0.7 to 11.2 W m^{-2} across different sub-regions during

447 the monsoon season and from 1.2 to 30.7 W m^{-2} during the non-monsoon season for BC externally

448 mixed with fresh snow spheres. The sub-regional variation increases to 1.4–37.7 W m^{-2} and 3.5–

449 58.4 W m^{-2} for aged snow during the monsoon and non-monsoon periods, respectively (Tables 3

450 and S4). In general, the spatiotemporal distribution of surface radiative effects follows that of snow

451 albedo reductions (Figs. 8a–8f). The impacts of snow nonsphericity and BC-snow internal mixing

452 on the surface radiative effects are similar to those on the albedo reductions discussed above. The

453 maximum surface radiative effect over the TP can reach up to 45.4 (79.9) W m^{-2} in NETP during

454 the non-monsoon season for BC internally mixed with fresh (aged) snow spheres (Tables 3 and

455 S4). The mean BC-induced snow albedo effects in the relatively clean TP areas (e.g., high-altitude

456 HIMA and SETP) are comparable to those over the Arctic and North American snowpack (Dang

457 et al., 2017; He et al., 2018a), while the effects in the contaminated TP areas (e.g., low-altitude

458 HIMA, CTP, SETP, and NETP) are generally similar to those in the low-elevation Alps (Painter

459 et al., 2013) and northern China snowpack (Wang et al., 2017).

460 Previous studies have shown accelerated snowmelt caused by BC-snow albedo effects in

461 the TP. For example, Yasunari et al. (2010) estimated that BC-induced albedo reductions over

Atmospheric
Chemistry
and Physics
Discussions

462   Himalayan glaciers could result in an extra snowmelt of 1–7 mm day^{-1} during the melting/summer

463   season. Qian et al. (2011) found a BC-induced snowmelt of up to 1.3 mm day^{-1} in late spring and

464   early summer averaged over the entire TP. Our results further suggest that the uncertainty

465   associated with snow shape and BC-snow mixing state could lead to a substantial variation in BC-

466   induced albedo reduction and hence snowmelt, which has significant implications for runoff and

467   water management in Asia. Accurate quantifications of the impact of snow grain shape and BC-

468   snow mixing state on snowmelt and subsequent hydrological processes require interactive land

469   surface and/or climate modeling, which will be investigated in future work.

470   We note that the present estimates of BC-induced snow albedo effects have uncertainties

471   and limitations. For example, different techniques have been used to measure BC concentration in

472   snow/ice, which may lead to discrepancies and inconsistency among observations and in model-

473   observation comparisons (Qian et al., 2015 and references therein). Besides, BC measurements

474   across the TP are from various sample types, such as surfaces of snowpack (with fresh/aged snow)

475   and glacier (with both snow/firn and granular ice), which may introduce uncertainty to the

476   understanding of BC contamination patterns (Zhang et al., 2017a; Li et al., 2018). In addition, in

477   the model, we do not account for the vertical variability of BC and snow grain properties in the TP

478   snowpack as well as some complex snowpack processes, including dynamic snow aging and

479   melting, post-depositional enrichment, and melting water scavenging, which may exert nontrivial

480   effects on BC-snow albedo effects (e.g., Flanner et al., 2007; Qian et al., 2014; Dang et al., 2017).

481   Improved estimates require comprehensive climate modeling coupled with the updated SNICAR

482   snow model and constrained by observed BC and snowpack conditions.

483

484   **5. Conclusions, implications, and future work**

485   We implemented a set of new BC-snow parameterizations into SNICAR, a widely used

486   snow albedo model, to account for the effects of snow nonsphericity and BC-snow internal mixing.

487   We evaluated model simulations by comparing with observations. We further applied the updated

488   SNICAR model with a comprehensive set of *in-situ* measurements of BC concentrations in the

489   Tibetan Plateau (TP) snowpack (glacier) to quantify the present-day BC-induced snow albedo

490   effects and associated uncertainties from snow grain shape and BC-snow mixing state.

491   We found that nonspherical snow grains tend to have higher albedos compared with

492   spherical snow grains, while BC-snow internal mixing leads to much larger albedo reductions

Atmospheric
Chemistry
and Physics
Discussions

493   relative to external mixing. The albedo reductions are weaker for nonspherical snow grains than

494   spherical grains, implying an important interactive effect from snow nonsphericity and internal

495   mixing. These results are consistent with previous studies (Flanner et al., 2012; Dang et al., 2016;

496   He et al., 2018a) and highlight the importance of concurrently accounting for snow grain shape

497   and aerosol-snow mixing state in snow albedo and climate modeling.

498   Comparisons with clean snow observations showed that model simulations using spherical

499   snow grains generally capture the observed spectral albedo but lead to a systematic underestimate

500   at NIR wavelengths, while assuming nonspherical snow grains improves model results. Further

501   evaluation with observed BC-contaminated snow albedo indicated that model simulations with the

502   combined effects of snow nonsphericity and BC-snow internal mixing perform better than those

503   with the common assumption of BC externally mixed with snow spheres.

504   We collected available *in-situ* observations of BC concentrations in snow/ice over the TP

505   during 2000–2015. We found that BC concentrations show distinct sub-regional and seasonal

506   variations. The concentrations are generally higher in the non-monsoon season and low-altitudes

507   (<5200 m) than in the monsoon season and high-altitudes (>5200 m), respectively. Among

508   different sub-regions, the high-altitude areas in the Himalayas and southeastern TP show the

509   lowest mean BC concentrations (<30 ppb) throughout the year, while the northeastern TP during

510   the non-monsoon season is most severely polluted by BC (>4000 ppb). The substantial

511   spatiotemporal heterogeneity of BC concentrations in the TP snowpack implies an urgent need for

512   more extensive measurements.

513   Based on the observed BC concentrations and snowpack properties, we conducted

514   SNICAR simulations to quantify the BC-induced snow albedo reductions and associated surface

515   radiative effects in different sub-regions and seasons. The spatiotemporal distribution of albedo

516   reductions generally follows that of BC concentrations, with stronger albedo reductions in the non-

517   monsoon period and low-altitude areas. We found that the effects of snow grain shape and BC-

518   snow mixing state become comparably important with the snow aging/size effect over severely

519   polluted areas. BC-snow internal mixing enhances the mean snow albedo reductions by 30–60%

520   relative to external mixing across different sub-regions and seasons, while nonspherical snow

521   grains weaken the albedo reductions by up to 31% relative to spherical grains. Therefore, the

522   combined effects of snow grain shape and BC-snow mixing state can complicate the

523   spatiotemporal features of BC-snow albedo reductions over the TP.

Atmospheric
Chemistry
and Physics
Discussions

524   We found that the BC-induced mean surface radiative effects can vary by up to an order of

525   magnitude across different sub-regions and seasons, showing a similar pattern with the snow

526   albedo reduction, with the effects further modified by snow grain shape and BC-snow mixing state.

527   The maximum effect can reach up to 45.4 (79.9) W m^{-2} in the northeastern TP during the non-

528   monsoon season, assuming BC-sphere internal mixing for fresh (aged) snow. The results suggest

529   that the uncertainty associated with snow shape and BC-snow mixing state over the TP could lead

530   to a large variation in BC-induced snowmelt, with significant implications for hydrological

531   processes and water management in Asia.

532   In summary, this study points toward an imperative need for extensive measurements and

533   improved model characterization of snow grain shape and aerosol-snow mixing state in order to

534   accurately estimate BC-induced snow albedo effects over the TP as well as other areas with highly

535   heterogeneous aerosol contamination and snowpack properties. In future work, we will incorporate

536   the new features of the updated SNICAR model into land surface and climate models, including

537   CESM-Community Land Model (CLM) for global modeling and WRF-Noah-MP for regional

538   modeling, to account for the effects of snow grain shape and aerosol-snow mixing state and to

539   assess the associated uncertainties and hydrological feedbacks in global/regional climate system.

540

541

542

546

547   *Author contributions.* CH designed and performed the parameterization implementation and

548   model simulations. MF offered data and help in developing model codes. FC and MB helped refine

549   model experiments. SK and JM provided black carbon observations. KNL and YQ gave valuable

550   comments. CH prepared the manuscript and all co-authors helped improve the manuscript.

551

553

Atmospheric
Chemistry
and Physics
Discussions

563

564

References

566   Aoki, T., Hachikubo, A., and Hori, M.: Effects of snow physical parameters on shortwave broadband albedos.
567   J. Geophys. Res., 108(D19), 4616, doi:10.1029/2003JD003506, 2003.
568   Aoki, T., K. Kuchiki, M. Niwano, Y. Kodama, M. Hosaka, and T. Tanaka: Physically based snow albedo model
569   for calculating broadband albedos and the solar heating profile in snowpack for general circulation models,
570   J. Geophys. Res., 116, D11114, doi:10.1029/2010JD015507, 2011.
571   Brandt, R. E., Warren, S. G., and Clarke, A. D.: A controlled snowmaking experiment testing the relation
572   between black carbon content and reduction of snow albedo, 116, D08109, doi:10.1029/2010JD015330,
573   2011.
574   Bond, T. C., and R. W. Bergstrom: Light absorption by carbonaceous particles: An investigative review, Aerosol
575   Sci. Technol., 40, 27–67, 2006.
576   Bond, T. C., Doherty, S. J., Fahey, D. W., Forster, P. M., Berntsen, T., DeAngelo, B. J., Flanner, M. G., Ghan,
577   S., Kärcher, B., Koch, D., Kinne, S., Kondo, Y., Quinn, P. K., Sarofim, M. C., Schultz, M. G., Schulz, M.,
578   Venkataraman, C., Zhang, H., Zhang, S., Bellouin, N., Guttikunda, S. K., Hopke, P. K., Jacobson, M. Z.,
579   Kaiser, J. W., Klimont, Z., Lohmann, U., Schwarz, J. P., Shindell, D., Storelvmo, T., Warren, S. G., and
580   Zender, C. S.: Bounding the role of black carbon in the climate system: A scientific assessment, J. Geophys.
581   Res.-Atmos., 118, 1–173, doi:10.1002/jgrd.50171, 2013.
582   Dang, C., Q. Fu, and S. Warren: Effect of Snow Grain Shape on Snow Albedo, J. Atmos. Sci., 73, 3573–
583   3583, doi: 10.1175/JAS-D-15-0276.1, 2016.
584   Dang, C., Warren, S. G., Fu, Q., Doherty, S. J., & Sturm, M.: Measurements of light-absorbing particles in snow
585   across the Arctic, North America, and China: Effects on surface albedo. Journal of Geophysical Research:
586   Atmospheres, 122, 10,149–10,168, doi:10.1002/2017JD027070, 2017.
587   Dentener, F., Kinne, S., Bond, T., Boucher, O., Cofala, J., Generoso, S., Ginoux, P., Gong, S., Hoelzemann, J.
588   J., Ito, A., Marelli, L., Penner, J. E., Putaud, J.-P., Textor, C., Schulz, M., van der Werf, G. R., and Wilson,
589   J.: Emissions of primary aerosol and precursor gases in the years 2000 and 1750 prescribed data-sets for
590   AeroCom, Atmos. Chem. Phys., 6, 4321–4344, doi:10.5194/acp-6-4321-2006, 2006.
591   Di Mauro, B., Baccolo, G., Garzonio, R., Giardino, C., Massabò, D., Piazzalunga, A., Rossini, M., and Colombo,
592   R.: Impact of impurities and cryoconite on the optical properties of the Morteratsch Glacier (Swiss Alps),
593   The Cryosphere, 11, 2393-2409, doi:10.5194/tc-11-2393-2017, 2017.

594 Dominé, F., T. Lauzier, A. Cabanes, L. Legagneux, W. F. Kuhs, K. Techmer, and T. Heinrichs: Snow
595   metamorphism as revealed by scanning electron microscopy, Micros. Res. Tech., 62, 33–48, 2003.
596 Flanner, M. G., Zender, C. S., Randerson, J. T., and Rasch, P. J.: Present-day climate forcing and response from
597   black carbon in snow, J. Geophys. Res.-Atmos., 112, D11202, doi:10.1029/2006jd008003, 2007.
598 Flanner, M. G., Zender, C. S., Hess, P. G., Mahowald, N. M., Painter, T. H., Ramanathan, V., and Rasch, P. J.:
599   Springtime warming and reduced snow cover from carbonaceous particles, Atmos. Chem. Phys., 9, 2481–
600   2497, doi:10.5194/acp-9-2481-2009, 2009.
601 Flanner, M. G., X. Liu, C. Zhou, J. E. Penner, and C. Jiao: Enhanced solar energy absorption by internally-mixed
602   black carbon in snow grains, Atmos. Chem. Phys., 12(10), 4699–4721, doi:10.5194/acp-12-4699-2012, 2012.
603 Flanner, M. G.: Arctic climate sensitivity to local black carbon, J. Geophys. Res.-Atmos., 118, 1840–1851,
604   doi:10.1002/jgrd.50176, 2013.
605 Fritsch, F. N. and R. E. Carlson: "Monotone Piecewise Cubic Interpolation," SIAM J. Numerical Analysis, 17,
606   238-246, 1980.
607 Fu, Q.: A new parameterization of an asymmetry factor of cirrus clouds for climate models. Journal of the
608   Atmospheric Sciences, 64, 4140–4150, doi:10.1175/2007JAS2289.1, 2007.
609 Fu, Q., W. B. Sun, and P. Yang: On modeling of scattering and absorption by nonspherical cirrus ice particles
610   in thermal infrared wavelengths. J. Atmos. Sci., 56, 2937–2947, doi:10.1175/1520-
611   0469(1999)056,2937:MOSAAB.2.0.CO;2, 1999.
612 Grenfell, T. C., Warren, S. G., and Mullen, P. C.: Reflection of solar radiation by the Antarctic snow surface at
613   ultraviolet, visible, and near-infrared wavelengths, J. Geophys. Res., 99, 18 669–18 684, 1994.
614 Grenfell, T. C., S. P. Neshyba, and S. G. Warren: Representation of a nonspherical ice particle by a collection
615   of independent spheres for scattering and absorption of radiation: 3. Hollow columns and plates. J. Geophys.
616   Res., 110, D17203, doi:10.1029/2005JD005811, 2005.
617 Hadley, O. L. and Kirchstetter, T. W.: Black-carbon reduction of snow albedo, Nat. Clim. Change, 2, 437–440,
618   doi:10.1038/NCLIMATE1433, 2012.
619 Hansen, J., and Nazarenko, L.: Soot climate forcing via snow and ice albedos, P. Natl. Acad. Sci. USA, 101,
620   423–428, doi:10.1073/pnas.2237157100, 2004.
621 He, C., Li, Q. B., Liou, K. N., Zhang, J., Qi, L., Mao, Y., Gao, M., Lu, Z., Streets, D. G., Zhang, Q., Sarin, M.
622   M., and Ram, K.: A global 3-D CTM evaluation of black carbon in the Tibetan Plateau, Atmos. Chem. Phys.,
623   14, 7091–7112, doi:10.5194/acp-14-7091-2014, 2014a.
624 He, C., Li, Q. B., Liou, K. N., Takano, Y., Gu, Y., Qi, L., Mao, Y. H., and Leung, L. R.: Black carbon radiative
625   forcing over the Tibetan Plateau, Geophys. Res. Lett., 41, 7806–7813, doi:10.1002/2014gl062191, 2014b.
626 He, C., K. N. Liou, Y. Takano, R. Zhang, M. Levy Zamora, P. Yang, Q. Li, and L. R. Leung: Variation of the
627   radiative properties during black carbon aging: theoretical and experimental intercomparison, Atmos. Chem.
628   Phys., 15(20), 11967-11980, doi:10.5194/acp-15-11967-2015, 2015.
629 He, C., Y. Takano, K.-N. Liou, P. Yang, Q. Li, and D. W. Mackowski: Intercomparison of the GOS approach,
630   superposition T-matrix method, and laboratory measurements for black carbon optical properties during
631   aging, J. Quant. Spectrosc. Radiat. Transfer., 184, 287–296, doi:10.1016/j.jqsrt.2016.08.004, 2016.
632 He, C., Y. Takano, and K.-N. Liou: Close packing effects on clean and dirty snow albedo and associated climatic
633   implications, Geophys. Res. Lett., 44, doi:10.1002/2017GL072916, 2017a.
634 He, C., Takano, Y., Liou, K.-N., Yang, P., Li, Q., and Chen, F.: Impact of snow grain shape and black carbon-
635   snow internal mixing on snow optical properties: Parameterizations for climate models. Journal of Climate,
636   30, 10,019–10,036, doi:10.1175/JCLI-D-17-0300.1, 2017b.
637 He, C., Liou, K.-N., Takano, Y., Yang, P., Qi, L., and Chen, F.: Impact of grain shape and multiple black carbon
638   internal mixing on snow albedo: Parameterization and radiative effect analysis. J. Geophys. Res.-Atmos.,
639   123, 1253–1268, doi:10.1002/2017JD027752, 2018a.

640 He, C., Liou, K.-N., and Takano, Y.: Resolving size distribution of black carbon internally mixed with snow:
641   Impact on snow optical properties and albedo. Geophysical Research Letters, 45, 2697–2705,
642   doi:10.1002/2018GL077062, 2018b.
643 Immerzeel, W. W., van Beek, L. P. H., and Bierkens, M. F. P.: Climate Change Will Affect the Asian Water
644   Towers, Science, 328, 1382–1385, doi:10.1126/science.1183188, 2010.
645 Jacobi, H.-W., Lim, S., Ménégoz, M., Ginot, P., Laj, P., Bonasoni, P., Stocchi, P., Marinoni, A., and Arnaud,
646   Y.: Black carbon in snow in the upper Himalayan Khumbu Valley, Nepal: observations and modeling of the
647   impact on snow albedo, melting, and radiative forcing, The Cryosphere, 9, 1685–1699, doi:10.5194/tc-9-
648   1685-2015, 2015.
649 Jacobson, M. Z.: Climate response of fossil fuel and biofuel soot, accounting for soot's feedback to snow and
650   sea ice albedo and emissivity, J. Geophys. Res.-Atmos., 109, D21201, doi:10.1029/2004jd004945, 2004.
651 Ji Z., S. Kang, Z. Cong, Q. Zhang, T. Yao: Simulation of carbonaceous aerosols over the Third Pole and adjacent
652   regions: distribution, transportation, deposition, and climatic effects, Climate Dynamics, 45(9-10), 2831-
653   2846, doi:10.1007/s00382-015-2509-1, 2015.
654 Kang, S., Xu, Y., You, Q., Flühel, W.-A., Pepin, N., and Yao, T.: Review of climate and cryosphere change in
655   the Tibetan Plateau, Environ. Res. Lett., 5, 015101, doi:10.1088/1748-9326/5/1/015101, 2010.
656 Kopacz, M., Mauzerall, D. L., Wang, J., Leibensperger, E. M., Henze, D. K., and Singh, K.: Origin and radiative
657   forcing of black carbon transported to the Himalayas and Tibetan Plateau, Atmos. Chem. Phys., 11, 2837–
658   2852, doi:10.5194/acp-11-2837-2011, 2011.
659 Kokhanovsky, A. A. and Zege, E. P.: Scattering optics of snow, Appl. Optics, 43, 1589–1602, 2004.
660 Kokhanovsky, A.: Spectral reflectance of solar light from dirty snow: a simple theoretical model and its
661   validation. The Cryosphere, 7, 1325–1331, doi:10.5194/tc-7-1325-2013, 2013.
662 Lee, W.-L., K. N. Liou, C. He, H.-C. Liang, T.-C. Wang, Q. Li, Z. Liu, and Q. Yue: Impact of absorbing aerosol
663   deposition on snow albedo reduction over the southern Tibetan plateau based on satellite observations, Theor.
664   Appl. Climatol., 129(3-4), 1373-1382, doi:10.1007/s00704-016-1860-4, 2017.
665 Li, C., Bosch, C., Kang, S., Andersson, A., Chen, P., Zhang, Q., Cong, Z., Chen, B., Qin, D., and Gustafsson,
666   Ö.: Sources of black carbon to the Himalayan-Tibetan Plateau glaciers, Nat. Commun., 7, 12574,
667   https://doi.org/10.1038/ncomms12574, 2016.
668 Li X. F., S. Kang, X. He, B. Qu, L. Tripathee, Z. Jing, R. Paudyal, Y. Li, Y. Zhang, F. Yan, G. Li, C. Li. Light-
669   absorbing impurities accelerate glacier melt in the Central Tibetan Plateau. Science of the Total Environment,
670   587-588: 482-490. Doi: 10.1016/j.scitotenv.2017.02.169, 2017.
671 Li X., S. Kang, G. Zhang, B. Que, L. Tripathea, R. Paudyal, Z. Jing, Y. Zhang, F. Yan, G. Li, X. Cui, R. Xu,
672   Z. Hu, C. Li. Light-absorbing impurities in a southern Tibetan Plateau glacier: Variations and potential impact
673   on snow albedo and radiative forcing. Atmospheric Research, 200, 77-87,
674   doi:10.1016/j.atmosres.2017.10.002, 2018.
675 Liou, K. N., Y. Takano, and P. Yang: Light absorption and scattering by aggregates: Application to black carbon
676   and snow grains, J. Quant. Spectrosc. Radiat. Transfer, 112(10), 1581–1594, doi:10.1016/j.jqsrt.2011.03.007,
677   2011.
678 Liou, K. N., Y. Takano, C. He, P. Yang, R. L. Leung, Y. Gu, and W. L. Lee: Stochastic parameterization for
679   light absorption by internally mixed BC/dust in snow grains for application to climate models, J. Geophys.
680   Res.-Atmos., 119, 7616–7632, doi:10.1002/2014JD021665, 2014.
681 Liou, K. N., and P. Yang: Light Scattering by Ice Crystals: Fundamentals and Applications, pp. 168–173,
682   Cambridge Univ. Press, Cambridge, U. K., 2016.
683 Lu, Z. F., Streets, D. G., Zhang, Q., and Wang, S.W.: A novel backtrajectory analysis of the origin of black
684   carbon transported to the Himalayas and Tibetan Plateau during 1996-2010, Geophys. Res. Lett., 39, L01809,
685   doi:10.1029/2011gl049903, 2012.

686 Manabe, S. and Terpstra, T. B.: The effects of mountains on the general circulation of the atmosphere as
687   identified by numerical experiments, J. Atmos. Sci., 31, 3–42, 1974.
688 Marshall, S. E.: A physical parameterization of snow albedo for use in climate models, NCAR Cooperative
689   Thesis 123 (175 pp.), Boulder, CO: National Center for Atmospheric Research, 1989.
690 McConnell, J. R., R. Edwards, G. L. Kok, M. G. Flanner, C. S. Zender, E. S. Saltzman, J. R. Banta, D. R.
691   Pasteris, M. M. Carter, and J. D. W. Kahl: 20th-century industrial black carbon emissions altered arctic
692   climate forcing, Science, 317, 1381–1384, doi:10.1126/science.1144856, 2007.
693 Meinander, O., Kazadzis, S., Arola, A., Riihelä, A., Räisänen, P., Kivi, R., Kontu, A., Kouznetsov, R., Sofiev,
694   M., Svensson, J., Suokanerva, H., Aaltonen, V., Manninen, T., Roujean, J.-L., and Hautecoeur, O.: Spectral
695   albedo of seasonal snow during intensive melt period at Sodankylä, beyond the Arctic Circle, Atmos. Chem.
696   Phys., 13, 3793-3810, doi:10.5194/acp-13-3793-2013, 2013.
697 Menon, S., Koch, D., Beig, G., Sahu, S., Fasullo, J., and Orlikowski, D.: Black carbon aerosols and the third
698   polar ice cap, Atmos. Chem. Phys., 10, 4559–4571, doi:10.5194/acp-10-4559-2010, 2010.
699 Ming, J., Cachier, H., Xiao, C., Qin, D., Kang, S., Hou, S., and Xu, J.: Black carbon record based on a shallow
700   Himalayan ice core and its climatic implications, Atmos. Chem. Phys., 8, 1343–1352, doi:10.5194/acp-8-
701   1343-2008, 2008.
702 Ming, J., Xiao, C. D., Cachier, H., Qin, D. H., Qin, X., Li, Z. Q., and Pu, J. C.: Black Carbon (BC) in the snow
703   of glaciers in west China and its potential effects on albedos, Atmos. Res., 92, 114–123,
704   doi:10.1016/j.atmosres.2008.09.007, 2009.
705 Ming, J., Xiao, C. D., Du, Z. C., and Yang, X. G.: An overview of black carbon deposition in High Asia glaciers
706   and its impacts on radiation balance, Advances in Water Resources, 55, 80–87,
707   doi:10.1016/j.advwatres.2012.05.015, 2013.
708 Niu, H.W., S.C. Kang, Y.L. Zhang, X.Y. Shi, X.F. Shi, S.J. Wang, et al.: Distribution of light-absorbing
709   impurities in snow of glacier on Mt. Yulong, southeastern Tibetan Plateau, Atmos. Res., 197, 474-484,
710   doi:10.1016/j.atmosres.2017.07.004, 2017.
711 Oleson, K., et al.: Technical description of version 4.5 of the Community Land Model (CLM). NCAR Technical
712   Note NCAR/TN-503+STR, 420 pp, doi:10.5065/D6RR1W7M, 2013.
713 Painter, T. H., Barrett, A. P., Landry, C. C., Neff, J. C., Cassidy, M. P., Lawrence, C. R., McBride, K. E., and
714   Farmer, G. L.: Impact of disturbed desert soils on duration of mountain snow cover, Geophys. Res. Lett., 34,
715   L12502, doi:10.1029/2007GL030284, 2007.
716 Painter, T. H., Flanner, M. G., Kaser, G., Marzeion, B., VanCuren, R. A., and Abdalati, W.: End of the Little Ice
717   Age in the Alps forced by industrial black carbon, P. Natl. Acad. Sci. USA, 110, 15216–15221,
718   doi:10.1073/pnas.1302570110, 2013.
719 Pedersen, C. A., J.-C. Gallet, J. Ström, S. Gerland, S. R. Hudson, S. Forsström, E. Isaksson, and T. K. Berntsen:
720   In situ observations of black carbon in snow and the corresponding spectral surface albedo reduction, J.
721   Geophys. Res. Atmos., 120, 1476–1489, doi:10.1002/2014JD022407, 2015.
722 Qian Y, WI Gustafson, Jr, LYR Leung, and SJ Ghan: Effects of soot-induced snow albedo change on snowpack
723   and hydrological cycle in western United States based on Weather Research and Forecasting chemistry and
724   regional climate simulations, Journal of Geophysical Research – Atmospheres, 114, D03108,
725   doi:10.1029/2008JD011039, 2009.
726 Qian, Y., Flanner, M. G., Leung, L. R., and Wang, W.: Sensitivity studies on the impacts of Tibetan Plateau
727   snowpack pollution on the Asian hydrological cycle and monsoon climate, Atmos. Chem. Phys., 11, 1929–
728   1948, doi:10.5194/acp-11-1929-2011, 2011.
729 Qian Y, H Wang, R Zhang, MG Flanner, and PJ Rasch: A Sensitivity Study on Modeling Black Carbon in Snow
730   and its Radiative Forcing over the Arctic and Northern China, Environmental Research Letters, 9(6), 064001,
731   doi:10.1088/1748-9326/9/6/064001, 2014.

732 Qian, Y., Yasunari, T. J., Doherty, S. J., Flanner, M. G., Lau, W. K., Ming, J., Wang, H., Wang, M., Warren, S.
733   G., and Zhang, R.: Light-absorbing particles in snow and ice: Measurement and modeling of climatic and
734   hydrological impact, Adv. Atmos. Sci., 32, 64–91, 2015.

735 Qin, D. H., Liu, S. Y., and Li, P. J.: Snow cover distribution, variability, and response to climate change in
736   western China, J. Clim., 19(9), 1820–1833, 2006.

737 Qu, B., Ming, J., Kang, S.-C., Zhang, G.-S., Li, Y.-W., Li, C.-D., Zhao, S.-Y., Ji, Z.-M., and Cao, J.-J.: The
738   decreasing albedo of the Zhadang glacier on western Nyainqentanglha and the role of light-absorbing
739   impurities, Atmos. Chem. Phys., 14, 11117-11128, doi:10.5194/acp-14-11117-2014, 2014.

740 Qu, X. and A. Hall: Assessing Snow Albedo Feedback in Simulated Climate Change. J. Climate, 19, 2617–
741   2630, doi:10.1175/JCLI3750.1, 2006.

742 Ramanathan, V., and Carmichael, G.: Global and regional climate changes due to black carbon, Nat. Geosci., 1,
743   221–227, doi:10.1038/Ngeo156, 2008.

744 Räisänen, P., Makkonen, R., Kirkevåg, A., and Debernard, J. B.: Effects of snow grain shape on climate
745   simulations: sensitivity tests with the Norwegian Earth System Model, The Cryosphere, 11, 2919-2942,
746   doi:10.5194/tc-11-2919-2017, 2017.

747 Schmale, J., Flanner, M., Kang, S., Sprenger, M., Zhang, Q., Guo, J., Li, Y., Schwikowski, M., and Farinotti,
748   D.: Modulation of snow reflectance and snowmelt from Central Asian glaciers by anthropogenic black
749   carbon, Sci. Rep.-UK, 7, 40501, doi:10.1038/srep40501, 2017.

750 Skiles, S. M. and Painter, T. H.: Daily evolution in dust and black carbon content, snow grain size, and snow
751   albedo during snowmelt, RockyMountains, Colorado, J. Glaciol., 63, 118–132, doi:10.1017/jog.2016.125,
752   2016.

753 Sterle, K. M., McConnell, J. R., Dozier, J., Edwards, R., and Flanner, M. G.: Retention and radiative forcing of
754   black carbon in eastern Sierra Nevada snow, The Cryosphere, 7, 365-374, doi:10.5194/tc-7-365-2013, 2013.

755 Svensson J., Virkkula A., Meinander O., Kivekäs N., Hannula H.-R., Järvinen O., Peltoniemi J.I., Gritsevich M.,
756   Heikkilä A., Kontu A., Neitola K., Brus D., Dagsson-Waldhauserova P., Anttila K., Vehkamäki M., Hienola
757   A., de Leeuw G., and Lihavainen H.: Soot-doped natural snow and its albedo–results from field experiments.
758   Boreal Env. Res. 21: 481–503, 2016.

759 Toon, O. B., McKay, C. P., Ackerman, T. P., and Santhanam, K.: Rapid calculation of radiative heating rates
760   and photodissociation rates in inhomogeneous multiple scattering atmospheres, J. Geophys. Res., 94, 16287–
761   16301, 1989.

762 Wang M, B Xu, J Cao, X Tie, H Wang, R Zhang, Y Qian, PJ Rasch, S Zhao, G Wu, H Zhao, DR Joswiak, J Li,
763   and Y Xie: Carbonaceous Aerosols Recorded in a Southeastern Tibetan Glacier: Analysis of Temporal
764   Variations and Model Estimates of Sources and Radiative Forcing, Atmos. Chem. Phys., 15, 1191-1204,
765   doi:10.5194/acp-15-1191-2015, 2015.

766 Wang, X., Doherty, S. J., and Huang, J.: Black carbon and other light-absorbing impurities in snow across
767   northern China, J. Geophys. Res. Atmos., 118, 1471–1492, doi:10.1029/2012JD018291, 2013.

768 Wang, X., Pu, W., Ren, Y., Zhang, X., Zhang, X., Shi, J., Jin, H., Dai, M., and Chen, Q.: Observations and model
769   simulations of snow albedo reduction in seasonal snow due to insoluble light-absorbing particles during 2014
770   Chinese survey, Atmos. Chem. Phys., 17, 2279-2296, doi:10.5194/acp-17-2279-2017, 2017.

771 Warren, S. G., and W. J. Wiscombe: A Model for the Spectral Albedo of Snow. 2. Snow Containing Atmospheric
772   Aerosols, J. Atmos. Sci., 37(12), 2734–2745, 1980.

773 Wiscombe, W. J., and Warren, S. G.: A model for the spectral albedo of snow: I. Pure snow. Journal of the
774   Atmospheric   Sciences,   37(12),   2712–2733,   doi:10.1175/1520-
775   0469(1980)037%3C2712:AMFTSA%3E2.0.CO;2, 1980.

Atmospheric
Chemistry
and Physics
Discussions

Open Access

776   Wu, L., Gu, Y., Jiang, J. H., Su, H., Yu, N., Zhao, C., Qian, Y., Zhao, B., Liou, K.-N., and Choi, Y.-S.: Impacts
777   of aerosols on seasonal precipitation and snowpack in California based on convection-permitting WRF-Chem
778   simulations, Atmos. Chem. Phys., 18, 5529-5547, doi:10.5194/acp-18-5529-2018, 2018.
779   Xu, B. Q., Cao, J. J., Hansen, J., Yao, T. D., Joswia, D. R., Wang, N. L., Wu, G. J., Wang, M., Zhao, H. B.,
780   Yang, W., Liu, X. Q., and He, J. Q.: Black soot and the survival of Tibetan glaciers, P. Natl. Acad. Sci. USA,
781   106, 22114–22118, doi:10.1073/pnas.0910444106, 2009.
782   Yang J., S. Kang, Z. Ji, D. Chen. Modeling the origin of anthropogenic black carbon and its climatic effect over
783   the Tibetan Plateau and surrounding regions. Journal of Geophysical Research: Atmospheres, 123. Doi:
784   10.1002/2017JD027282, 2018.
785   Yang, S., B. Xu, J. Cao, C. S. Zender, and M. Wang: Climate effect of black carbon aerosol in a TP glacier,
786   Atmos. Environ., 111, 71–78, doi:10.1016/j.atmosenv.2015.03.016, 2015.
787   Yao, T., Thompson, L. G., Mosbrugger, V., Zhang, F., Ma, Y., Luo, T., Xu, B., Yang, X., Joswiak, D. R., Wang,
788   W., Joswiak, M. E., Devkota, L. P., Tayal, S., Jilani, R., and Fayziev, R.: Third Pole Environment (TPE),
789   Environ. Dev., 3, 52–64, doi:10.1016/j.envdev.2012.04.002, 2012.
790   Yasunari, T. J., Bonasoni, P., Laj, P., Fujita, K., Vuillermoz, E., Marinoni, A., Cristofanelli, P., Duchi, R., Tartari,
791   G., and Lau, K. M.: Estimated impact of black carbon deposition during premonsoon season from Nepal
792   Climate Observatory – Pyramid data and snow albedo changes over Himalayan glaciers, Atmos. Chem.
793   Phys., 10, 6603–6615, doi:10.5194/acp-10-6603-2010, 2010.
794   Yeh, T.-C., Gao, Y. X., Tang, M. C., Luo, S. W., Shen, C. B., Gao, D. Y., Song, Z. S., Qian, Y. F., Yuan, F. M.,
795   Li, G. Q., Ding, Y. H., Chen, Z. T., Zhou, M. Y., Yang, K. J., and Wang, Q. Q.: Meteorology of Qinhai-
796   Xizhang (Tibetan) Plateau, Science Press, Beijing, 300 pp., 1979 (in Chinese).
797   Yu, F. and Luo, G.: Simulation of particle size distribution with a global aerosol model: contribution of
798   nucleation to aerosol and CCN number concentrations, Atmos. Chem. Phys., 9, 7691–7710, doi:10.5194/acp-
799   9-7691-2009, 2009.
800   Zhao, C., Hu, Z., Qian, Y., Ruby Leung, L., Huang, J., Huang, M., Jin, J., Flanner, M. G., Zhang, R., Wang, H.,
801   Yan, H., Lu, Z., and Streets, D. G.: Simulating black carbon and dust and their radiative forcing in seasonal
802   snow: a case study over North China with field campaign measurements, Atmos. Chem. Phys., 14, 11475-
803   11491, doi:10.5194/acp-14-11475-2014, 2014.
804   Zhang, R., Wang, H., Qian, Y., Rasch, P. J., Easter, R. C., Ma, P.-L., Singh, B., Huang, J., and Fu, Q.:
805   Quantifying sources, transport, deposition, and radiative forcing of black carbon over the Himalayas and
806   Tibetan Plateau, Atmos. Chem. Phys., 15, 6205-6223, doi:10.5194/acp-15-6205-2015, 2015.
807   Zhang Y.L., S. Kang, Z. Cong, J. Schmale, M. Sprenger, C. Li, W. Yang, T. Gao, M. Sillanpää, X. Li, Y. Liu,
808   P. Chen, X. Zhang. Light-absorbing impurities enhance glacier albedo reduction in the southeastern Tibetan
809   Plateau. Journal of Geophysical Research - Atmosphere, 122. Doi: 10.1002/2016JD026397, 2017a.
810   Zhang Y. L., S. Kang, C. Li, T. Gao, Z. Cong, M. Sprenger, Y. Liu, X. Li, J. Guo, M. Sillanpää, K. Wang, J.
811   Chen, Y. Li, S. Sun: Characteristics of black carbon in snow from Laohugou No. 12 glacier on the northern
812   Tibetan   Plateau,   Science   of   the   Total   Environment,   607-608,   1237-1249,
813   doi:10.1016/j.scitotenv.2017.07.100, 2017b.
814   Zhang, Y., Kang, S., Sprenger, M., Cong, Z., Gao, T., Li, C., Tao, S., Li, X., Zhong, X., Xu, M., Meng, W.,
815   Neupane, B., Qin, X., and Sillanpää, M.: Black carbon and mineral dust in snow cover on the Tibetan Plateau,
816   The Cryosphere, 12, 413-431, doi:10.5194/tc-12-413-2018, 2018.
817
818
819
820
821

Atmospheric
Chemistry
and Physics
Discussions

822 **Table 1.** Parameter values used in SNICAR simulations when comparing with observed snow
823 albedo (see Figs. 6 and 7). The observed snowpack properties are used in each case when they are
824 available. Four types of snow shapes (sphere, spheroid, hexagonal plate, and Koch snowflake)
825 and/or two types of BC-snow mixing (internal and external) are assumed in the simulations.
826

Observational cases		Model parameters							
References	Type	Radiation	Solar zenith angle	Underlying ground albedo	Snow layer	Snow thickness (cm)	Snow effective radius (µm)	Snow density (kg m^{-3})	BC content (ppb)
Pure snow									
Hadley and Kirchstetter 2012	laboratory measurement	direct	0°	0	1	semi-infinite	55/65/110	550	
Brandt et al. 2011	open-field experiment	diffuse		0*	2	15 40	80/95/140/160 500*	150 300	0
Painter et al. 2007	field measurement	diffuse		0*	1	100	600	350	
Grenfell et al. 1994	field measurement	diffuse		0.6	multiple layers with layer-specific properties (see reference for details)				
BC-contaminated snow									
Pedersen et al. 2015	field measurement	diffuse		0.2	1	multiple cases with case-specific properties (see reference for details)		150*	case-specific (see reference for details)
Svensson et al. 2016	open-field experiment	direct	61.3°	0.1	multiple layers with layer-specific snow properties & vertically averaged BC concentrations (see reference for details)				232/489/554/ 1030/6420
Meinander et al. 2013	field measurement	direct	55°	0*	2	0.5 9.5	1000 5000	350 350	87.1
Brandt et al. 2011	open-field experiment	diffuse		0*	2	15 40	80/95/140/160 500*	150 300	2250 20
Hadley and Kirchstetter 2012	laboratory measurement	direct	0°	0	1	semi-infinite	55/65/110	550	110/450/860/ 1680

827 *The parameters are assumed in simulations due to the lack of measurements.

828
829
830
831
832
833
834

Atmospheric
Chemistry
and Physics
Discussions

835 **Table 2.** Regional and seasonal mean BC-induced all-sky snow albedo reductions for fresh snow
836 over the Tibetan Plateau during 2000–2015. See Table S3 for results of aged snow.

Region[1]		Season	BC mean content (ppb)	Fresh snow (R_e = 100 μm)							
				External mixing				Internal mixing			
				Sphere	Spheroid	Hexagonal plate	Koch snowflake	Sphere	Spheroid	Hexagonal plate	Koch snowflake
HIMA	high alt. low alt.	monsoon	16.3	0.005	0.005	0.004	0.004	0.007	0.006	0.005	0.005
	high alt. low alt.	non-monsoon	29.4 1151.8	0.008 0.066	0.007 0.061	0.006 0.052	0.006 0.049	0.011 0.098	0.010 0.091	0.008 0.077	0.007 0.072
	high alt. low alt.	annual	17.5	0.006	0.005	0.004	0.004	0.008	0.007	0.006	0.005
CTP	high alt. low alt.	monsoon	63.2 446.0	0.014 0.047	0.012 0.043	0.010 0.036	0.009 0.033	0.018 0.065	0.016 0.060	0.014 0.050	0.012 0.046
	high alt. low alt.	non-monsoon	331.6 1632.9	0.034 0.077	0.031 0.071	0.026 0.061	0.023 0.057	0.047 0.114	0.043 0.106	0.036 0.091	0.033 0.084
	high alt. low alt.	annual	146.3 263.5	0.021 0.034	0.019 0.031	0.016 0.026	0.014 0.024	0.028 0.047	0.026 0.043	0.021 0.035	0.019 0.033
NWTP	high alt. low alt.	monsoon	143.6 272.2	0.023 0.035	0.021 0.032	0.017 0.026	0.016 0.024	0.030 0.048	0.027 0.044	0.023 0.036	0.021 0.033
	high alt. low alt.	non-monsoon	61.1 64.7	0.014 0.014	0.013 0.013	0.011 0.011	0.010 0.010	0.018 0.018	0.017 0.017	0.014 0.014	0.013 0.013
	high alt. low alt.	annual	87.4 191.4	0.016 0.028	0.015 0.026	0.012 0.021	0.011 0.020	0.022 0.038	0.020 0.035	0.016 0.029	0.015 0.026
NETP	high alt. low alt.	monsoon	190.9	0.023	0.021	0.017	0.016	0.031	0.029	0.024	0.022
	high alt. low alt.	non-monsoon	4323.2	0.151	0.140	0.118	0.110	0.223	0.208	0.178	0.165
	high alt. low alt.	annual	823.0	0.066	0.061	0.051	0.047	0.095	0.087	0.072	0.067
SETP	high alt. low alt.	monsoon	5.2 263.6	0.003 0.032	0.002 0.029	0.002 0.024	0.002 0.022	0.004 0.043	0.003 0.040	0.003 0.033	0.003 0.030
	high alt. low alt.	non-monsoon	13.7 1110.9	0.005 0.067	0.005 0.062	0.004 0.052	0.004 0.048	0.007 0.098	0.006 0.090	0.005 0.077	0.005 0.071
	high alt. low alt.	annual	9.0 249.4	0.004 0.031	0.004 0.028	0.003 0.023	0.003 0.021	0.005 0.042	0.005 0.039	0.004 0.032	0.004 0.029
NOTP	high alt. low alt.	monsoon	368.6	0.040	0.036	0.030	0.028	0.055	0.050	0.042	0.038
	high alt. low alt.	non-monsoon	89.1	0.018	0.016	0.013	0.012	0.023	0.021	0.017	0.016
	high alt. low alt.	annual	138.3	0.024	0.022	0.018	0.016	0.031	0.028	0.024	0.022

837 [1]Six sub-regions: Himalayas (HIMA), central Tibetan Plateau (CTP), northwestern Tibetan Plateau (NWTP),
838 northeastern Tibetan Plateau (NETP), southeastern Tibetan Plateau (SETP), and north of Tibetan Plateau (NOTP).
839 Each sub-region is further divided into high (>5200 m) and low (<5200 m) altitudes.
840
841
842
843
844
845
846
847
848

849   **Table 3.** Regional and seasonal mean BC-induced all-sky surface radiative effects (W m^{-2}) for
850   fresh snow over the Tibetan Plateau during 2000–2015. See Table S4 for results of aged snow.

Region[1]		Season	Fresh snow ($R_e = 100$ μm)							
			External mixing				Internal mixing			
			Sphere	Spheroid	Hexagonal plate	Koch snowflake	Sphere	Spheroid	Hexagonal plate	Koch snowflake
HIMA	high alt.	monsoon	1.4	1.3	1.1	1.0	2.0	1.8	1.5	1.4
	low alt.									
	high alt.	non-monsoon	2.0	1.8	1.5	1.4	2.6	2.4	2.0	1.8
	low alt.		16.2	15.0	12.8	11.9	23.9	22.2	19.0	17.6
	high alt.	annual	1.5	1.4	1.2	1.1	2.0	1.8	1.5	1.4
	low alt.									
CTP	high alt.	monsoon	4.2	3.9	3.2	3.0	5.6	5.1	4.2	3.9
	low alt.		14.7	13.5	11.2	10.3	20.5	18.7	15.6	14.3
	high alt.	non-monsoon	7.7	7.0	5.8	5.3	10.6	9.7	8.1	7.4
	low alt.		17.3	16.2	13.8	12.8	25.8	24.1	20.6	19.1
	high alt.	annual	5.3	4.9	4.0	3.7	7.2	6.6	5.4	5.0
	low alt.		8.7	8.0	6.6	6.1	11.9	10.9	9.1	8.3
NWTP	high alt.	monsoon	7.2	6.6	5.5	5.0	9.7	8.8	7.3	6.7
	low alt.		11.3	10.3	8.5	7.8	15.3	14.0	11.6	10.7
	high alt.	non-monsoon	2.7	2.5	2.1	1.9	3.6	3.2	2.7	2.4
	low alt.		2.7	2.5	2.1	1.9	3.6	3.3	2.7	2.5
	high alt.	annual	3.9	3.5	2.9	2.7	5.1	4.7	3.9	3.5
	low alt.		6.6	6.1	5.0	4.6	9.0	8.2	6.8	6.2
NETP	high alt.	monsoon	6.5	6.0	5.0	4.6	8.9	8.2	6.8	6.3
	low alt.									
	high alt.	non-monsoon	30.7	28.4	24.1	22.3	45.4	42.3	36.2	33.6
	low alt.									
	high alt.	annual	15.3	14.0	11.7	10.7	21.8	20.0	16.7	15.4
	low alt.									
SETP	high alt.	monsoon	0.7	0.6	0.5	0.5	1.0	0.9	0.8	0.7
	low alt.		8.5	7.7	6.4	5.9	11.5	10.6	8.8	8.0
	high alt.	non-monsoon	1.2	1.1	0.9	0.8	1.5	1.4	1.1	1.0
	low alt.		14.5	13.4	11.4	10.5	21.3	19.7	16.6	15.4
	high alt.	annual	0.9	0.8	0.7	0.6	1.3	1.2	1.0	0.9
	low alt.		7.3	6.6	5.5	5.0	9.9	9.0	7.5	6.9
NOTP	high alt.	monsoon	11.2	10.2	8.4	7.7	15.4	14.1	11.7	10.7
	low alt.									
	high alt.	non-monsoon	2.9	2.7	2.2	2.0	3.8	3.5	2.9	2.6
	low alt.									
	high alt.	annual	4.8	4.4	3.6	3.3	6.4	5.8	4.8	4.4
	low alt.									

851   [1]Six sub-regions: Himalayas (HIMA), central Tibetan Plateau (CTP), northwestern Tibetan Plateau (NWTP),
852   northeastern Tibetan Plateau (NETP), southeastern Tibetan Plateau (SETP), and north of Tibetan Plateau (NOTP).
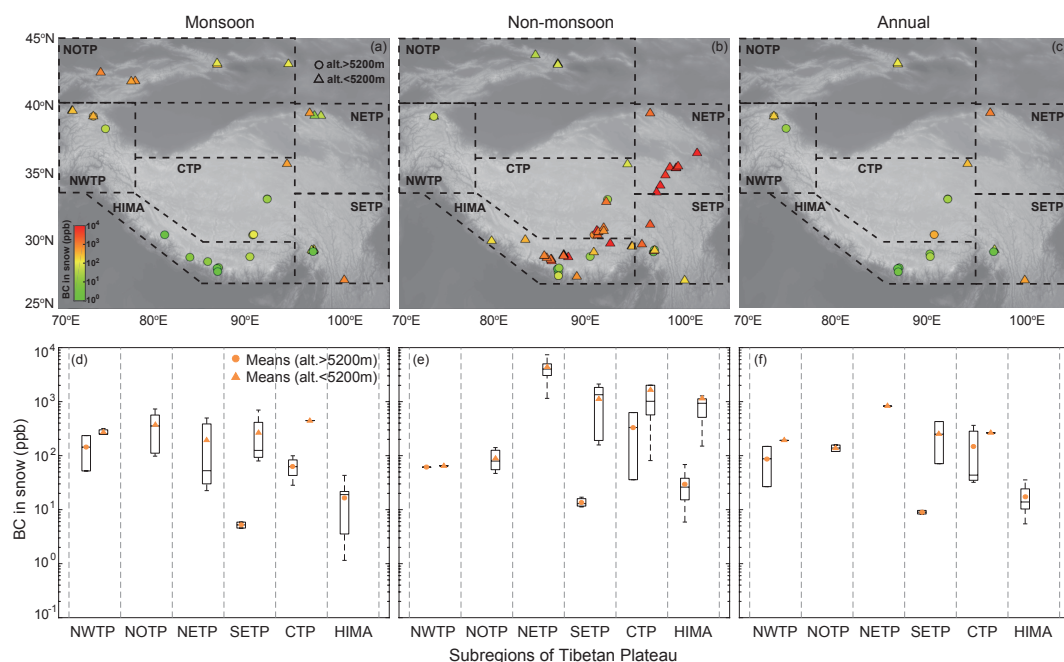853   Each sub-region is further divided into high (>5200 m) and low (<5200 m) altitudes.
854
855
856
857
858
859
860
861

862
863
Figure 1. Observed BC concentrations in snow over the Tibetan Plateau (TP) during (a, d) monsoon, (b, e) non-monsoon, and (c, f) annual periods in 2000–2015 (see Table S1 for details). (a–c) Spatial distributions of seasonal mean BC concentrations at altitudes >5200 m (circles) and <5200 m (triangles) in six sub-regions, including northwestern TP (NWTP), north of TP (NOTP), northeastern TP (NETP), southeastern TP (SETP), central TP (CTP), and Himalayas (HIMA). (d–f) Boxplots of observed BC concentrations in snow (shown in a–c) within each sub-region, with medians (middle bars), interquartile ranges (between 25th and 75th percentiles; boxes), and maxima/minima (whiskers) within ±1.5 × interquartile ranges. Some boxplots are shrunk due to limited samples. Results for altitudes >5200 m and <5200 m are shown as left and right boxplots within each sub-region, respectively, with circles and triangles indicating mean values. Note that some sub-regions only have observations at altitudes >5200 m or <5200 m.

875
876
877
878
879
880
881
882
883
884
885
886
887
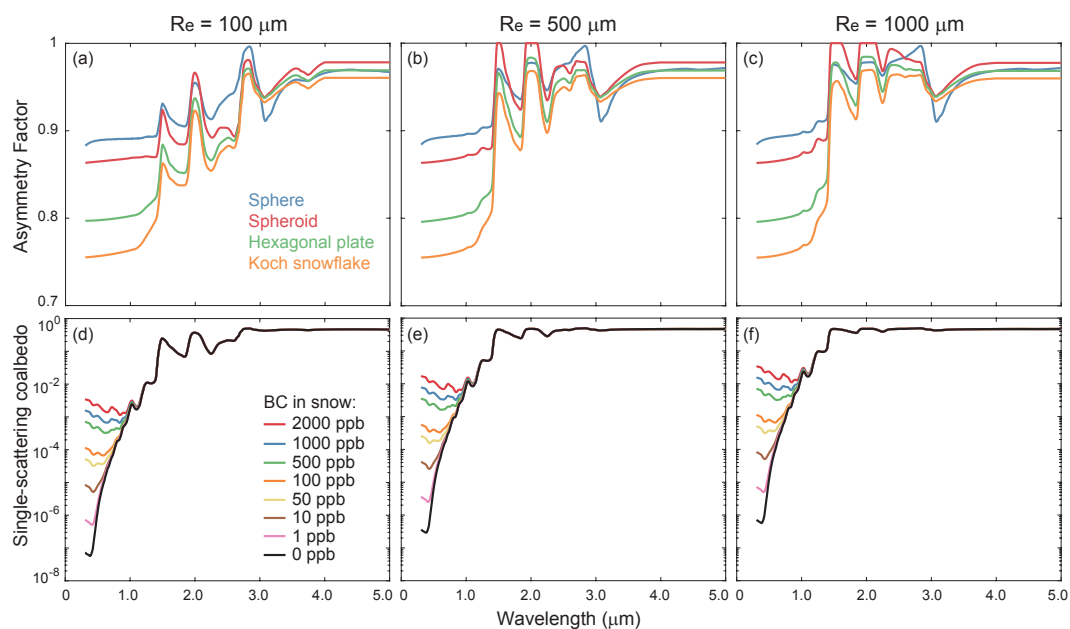
Figure 2. (a–c) Spectral (0.3–5 μm) asymmetry factors of pure snow with effective radii (R_e) of (a) 100, (b) 500, and (c) 1000 μm for sphere (blue), spheroid (red), hexagonal plate (green), and Koch snowflake (orange) derived from the updated SNICAR model. (d–f) Spectral single-scattering coalbedo of snow grains internally mixed with different BC concentrations (indicated by different colors) for snow effective radii (R_e) of (d) 100, (e) 500, and (f) 1000 μm derived from the updated SNICAR model. Note that the y-axes in (d–f) are in logarithmic scales.

888
889
890
891
892
893
894
895
896
897
898
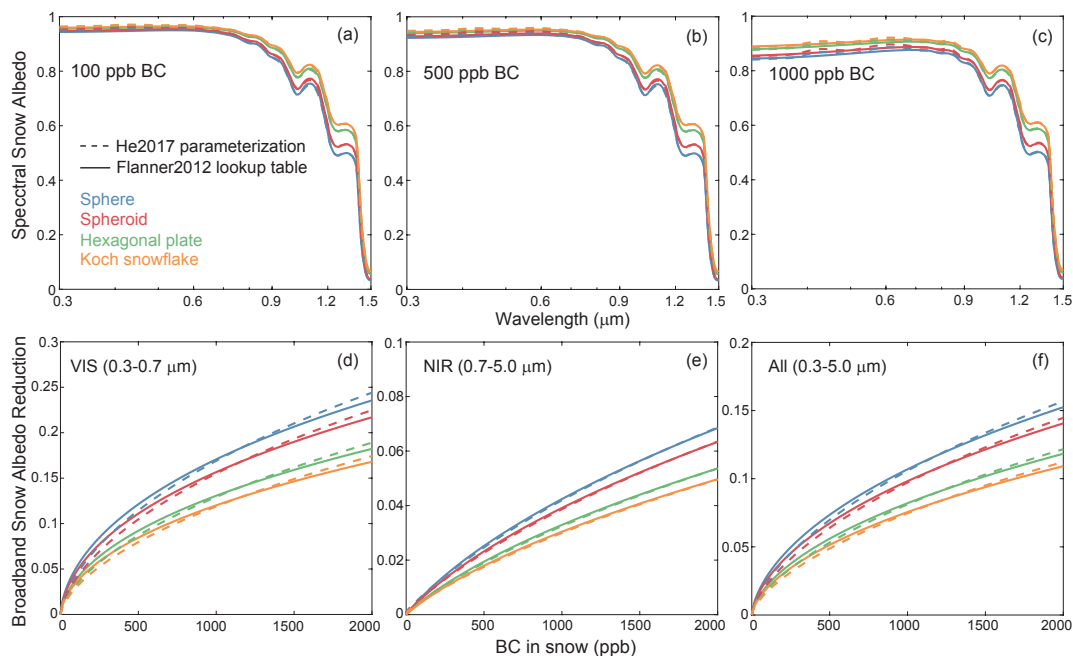899
900
901
902
903
904
905
906
907
908
909
910
911
912
913
914
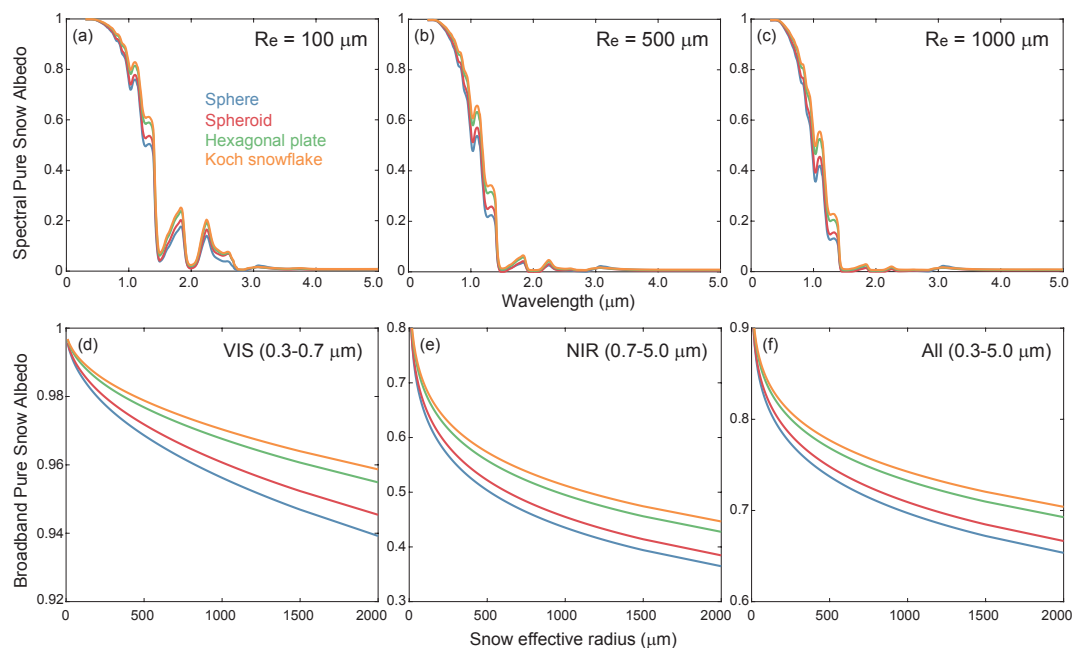
915
916
Figure 3. (a–c) Spectral (0.3–5 μm) direct-beam albedo of pure semi-infinite snow layers with
effective radii (R_e) of (a) 100, (b) 500, and (c) 1000 μm for sphere (blue), spheroid (red), hexagonal
plate (green), and Koch snowflake (orange) based on the updated SNICAR model. (d–f) Same as
(a–c), but for broadband albedo as a function of snow effective radius (R_e) at (d) visible (VIS, 0.3–
0.7 μm), (e) near-infrared (NIR, 0.7–5 μm), and (f) all (0.3–5 μm) wavelengths. The results for
diffuse snow albedo are shown in Fig. S1.

923
924
925
926
927
928
929
930
931
932
933
934
935
936
937
938
939
940
941
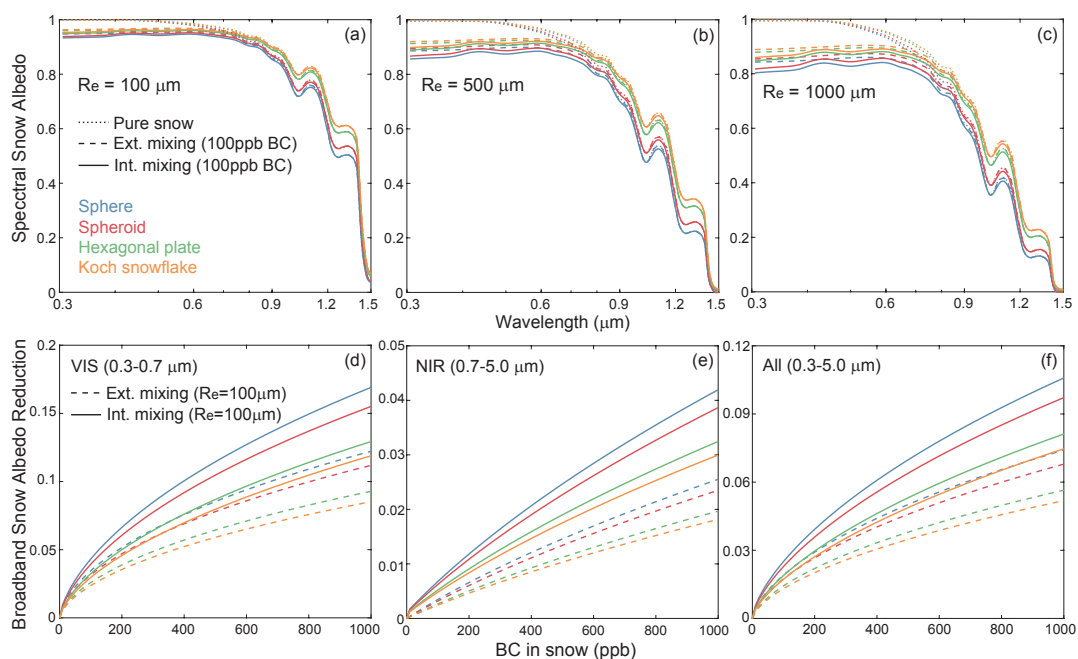
942
943
944 **Figure 4.** (a–c) Spectral (0.3–1.5 μm) direct-beam albedo of semi-infinite snow layers with
945 effective radii (R_e) of (a) 100, (b) 500, and (c) 1000 μm for pure snow (dotted lines), snow
946 externally mixed with 100 ppb BC (dashed lines), and snow internally mixed with 100 ppb BC
947 (solid lines) with shapes of sphere (blue), spheroid (red), hexagonal plate (green), and Koch
948 snowflake (orange) based on the updated SNICAR model. The results for 1000 ppb BC and diffuse
949 snow albedo are shown in Fig. S2. (d–f) Same as (a–c), but for broadband albedo reduction as a
950 function of BC concentration in snow with R_e of 100 μm at (d) visible (VIS, 0.3–0.7 μm), (e) near-
951 infrared (NIR, 0.7–5 μm), and (f) all (0.3–5 μm) wavelengths. The results for snow with R_e of 500
952 and 1000 μm and diffuse albedo reductions are shown in Figs. S3 and S4, respectively.
953
954
955
956
957
958
959
960
961
962
963
964
965
966
967

Atmospheric
Chemistry
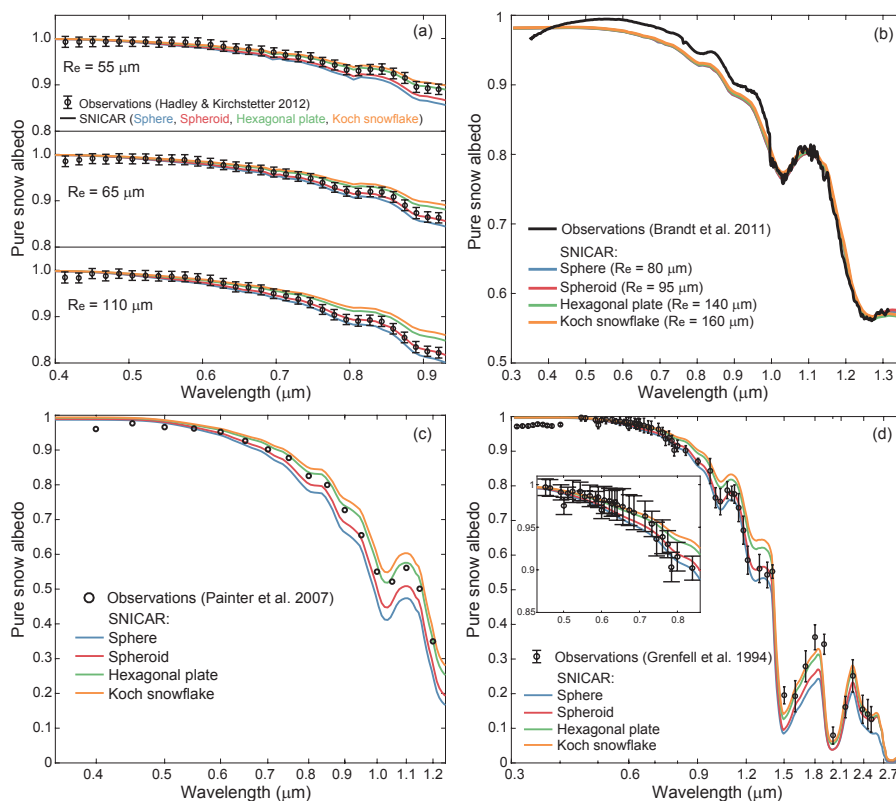and Physics
Discussions

968
969
970 **Figure 5.** Comparisons of SNICAR simulated direct-beam albedo of semi-infinite snow layers
971 between using the Flanner et al. (2012) lookup table (solid lines) and the He et al. (2017b)
972 parameterization (dashed lines) for BC internally mixed with snow grains with an effective radius
973 of 100 μm for sphere (blue), spheroid (red), hexagonal plate (green), and Koch snowflake (orange).
974 (a–c) Spectral (0.3–1.5 μm) snow albedo for BC concentrations of (a) 100, (b) 500, and (c) 1000
975 ppb. (d–f) Broadband snow albedo reduction as a function of BC concentration in snow at (d)
976 visible (VIS, 0.3–0.7 μm), (e) near-infrared (NIR, 0.7–5 μm), and (f) all (0.3–5 μm) wavelengths.
977 The results for snow effective radii of 500 and 1000 μm are shown in Figs. S5 and S6, respectively.
978
979
980
981
982
983
984
985
986
987
988
989
990
991
992
993

Atmospheric
Chemistry
and Physics
Discussions

Figure 6. Comparisons of spectral pure snow albedo from observations (black) and SNICAR
simulations using observed snowpack properties (see Table 1) and assuming sphere (blue),
spheroid (red), hexagonal plate (green), and Koch snowflake (orange). (a) Observations are
obtained from laboratory measurements (Hadley and Kirchstetter, 2012). (b) Observations are
obtained from open-field experiments in New York (Brandt et al., 2011). The effective radii (R_e)
for each snow shape are obtained to best match observations at wavelengths of 1−1.3 μm. (c)
Observations are obtained from field measurements over Rocky Mountains (Painter et al., 2007).
(d) Observations are obtained from field measurements at the South Pole (Grenfell et al., 1994).
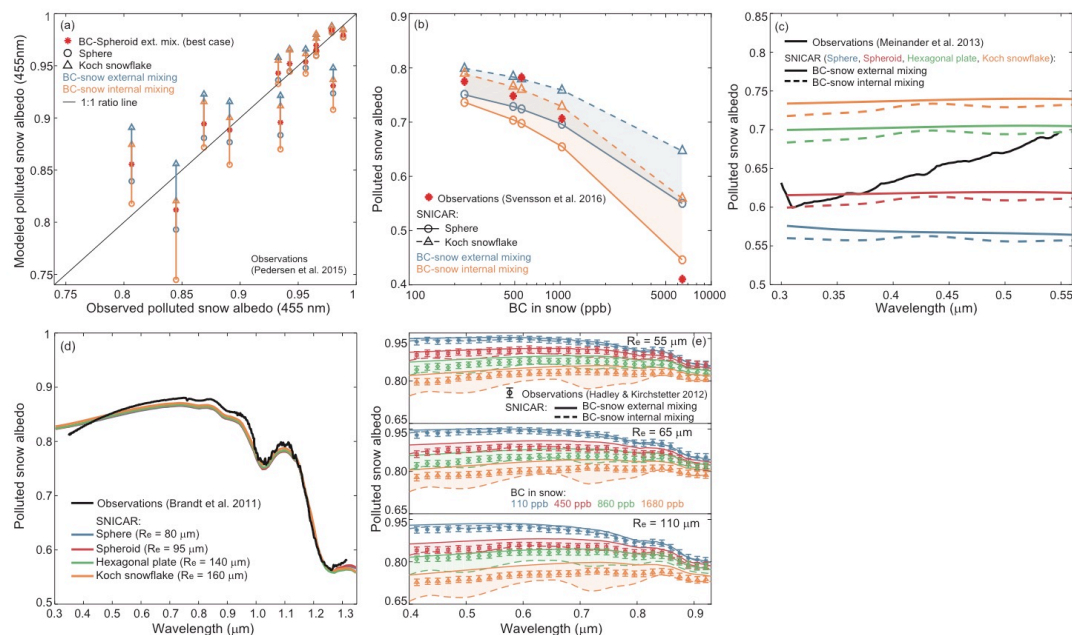
Figure 7. Comparisons of BC-polluted snow albedo from observations and SNICAR simulations using observed snowpack properties (see Table 1). (a) Observations (x-axis) are obtained from field measurements in the Arctic (Pedersen et al., 2015). Model results (y-axis) for spheres (circles) and Koch snowflake (triangles) are shown as lower and upper limits for shape effects, along with BC-snow external (blue) and internal (orange) mixing. Also shown is the best case (red asterisks; BC-spheroid external mixing) that matches observations. (b) Observations (red asterisks; broadband albedo for 0.285–2.8 μm) are obtained from open-field experiments in Finland (Svensson et al., 2016). Model results for spheres (circles) and Koch snowflake (triangles) are shown as lower and upper limits for shape effects, along with BC-snow external (blue) and internal (orange) mixing. (c) Observations (black lines) are obtained from field measurements in the European Arctic (Meinander et al., 2013). Model results assuming sphere (blue), spheroid (red), hexagonal plate (green), and Koch snowflake (orange) along with BC-snow external (dashed lines) and internal (solid lines) are shown. (d) Observations (black) are obtained from open-field experiments in New York (Brandt et al., 2011). BC is assumed to be externally mixed with snow spheres (blue), spheroids (red), hexagonal plates (green), and Koch snowflakes (orange). The effective radii (R_e) for each snow shape are obtained to best match observations at wavelengths of 1–1.3 μm. (e) Observations (circles) are obtained from laboratory measurements (Hadley and Kirchstetter, 2012). BC is assumed to be externally (solid lines) and internally (dashed lines) mixed with snow spheres.
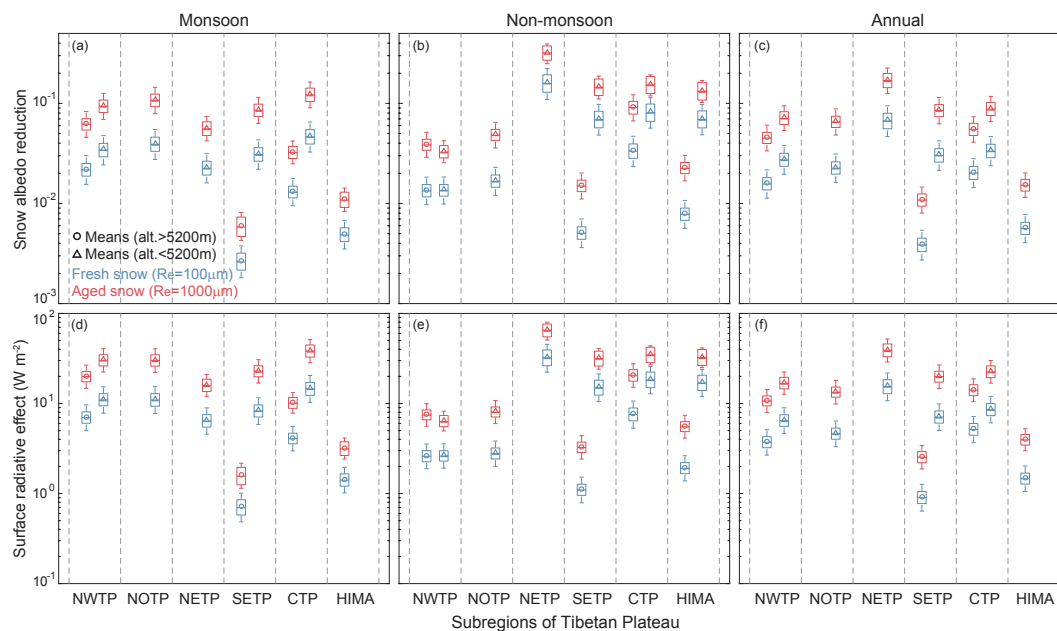
Atmospheric
Chemistry
and Physics
Discussions

Figure 8. Regional and seasonal mean BC-induced all-sky snow albedo reductions and surface radiative effects during (a, d) monsoon, (b, e) non-monsoon, and (c, f) annual periods in 2000–2015 over six Tibetan Plateau (TP) sub-regions (see Fig. 1), including northwestern TP (NWTP), north of TP (NOTP), northeastern TP (NETP), southeastern TP (SETP), central TP (CTP), and Himalayas (HIMA). (a–c) Boxplots of mean snow albedo reductions within each sub-region based on SNICAR simulations using the observed BC concentrations in snow (Fig. 1), snow thicknesses, and snow densities (see text for details). Results for altitudes >5200 m and <5200 m are shown as left and right boxplots within each sub-region, respectively, with circles and triangles indicating mean values. Model results assume BC externally and internally mixed with spheres, spheroids, hexagonal plates, and Koch snowflakes for fresh (blue, $R_e = 100$ μm) and aged (red, $R_e = 1000$ μm) snow. Each data point used for the boxplot is the sub-regional average assuming a type of snow shape and BC-snow mixing, and hence the boxplot indicates the variation caused by effects of snow shape and BC-snow mixing state. Note that some sub-regions only have BC observations at altitudes >5200 m or <5200 m (see Fig. 1). (d–f) Same as (a–c), but for BC-induced all-sky surface radiative effects caused by the snow albedo reductions shown in (a–c). Calculations use the surface downward solar radiation and cloud cover fraction from the MERRA-2 reanalysis fields (see text and Table S2 for details).